INAR
INSTITUTE FOR ATMOSPHERIC AND EARTH SYSTEM RESEARCH

Master's thesis
Master's Programme in Atmospheric Sciences
Geophysics of the Hydrosphere

Observed Changes in the Hydrography of the Arctic Ocean

Laura I. S. Rautiainen

March 12, 2020

Supervisor(s): professor Petteri Uotila

Examiner(s): docent Ekaterina Ezhova
professor Petteri Uotila

University of Helsinki
Faculty of Science

PL 64 (Gustaf Hällströmin katu 2a)
00014 Helsingin yliopisto

HELSINGIN YLIOPISTO — HELSINGFORS UNIVERSITET — UNIVERSITY OF HELSINKI

Tiedekunta — Fakultet — Faculty	Koulutusohjelma — Utbildningsprogram — Degree programme
Faculty of Science	Master's Programme in Atmospheric Sciences Geophysics of the Hydrosphere

Tekijä — Författare — Author

Laura I. S. Rautiainen

Työn nimi — Arbetets titel — Title

Observed Changes in the Hydrography of the Arctic Ocean

Työn laji — Arbetets art — Level	Aika — Datum — Month and year	Sivumäärä — Sidantal — Number of pages
Master's thesis	March 12, 2020	72

Tiivistelmä — Referat — Abstract

Ocean reanalysis products (ORAs) can provide information on the state of the ocean. Although the different data sources, model configurations, forcing choices and assimilation methods cause the ORAs to deviate from each other, the ensemble approach has been previously found to produce realistic mean states. This raises the question if ORAs could be used for studying temporal and spatial changes in the Arctic Ocean, where measurements are generally sparse. Such study has not been previously published. In this thesis, the changes in the hydrography of the Arctic Ocean are examined over the previous decades based on selected ORAs.

Eleven ORAs, TOPAZ4, C-GLORS025v5, ECDA3, GECCO2, GLORYS2v4, GloSea5-GO5, MOVE-G2i, ORAP5, SODA3.3.1, UR025.4 and ORAS5, were chosen for this study due to their overlap over 1993–2010 and the multimodel ensemble (MMM) was formulated based on the products, excluding ECDA3. The data were divided into depth layers and layer-average salinities and temperatures were used to calculate basin-average anomaly time series and trends to study the observed temporal changes. Per-grid trends were also produced to study both spatial and temporal changes in more detail. To assess their reliability, trends from the MMM and individual ORAs were compared to an observational product, EN4.2.0.g10 and the variability in the products and the MMM was assessed using statistical measures.

The Eurasian Basin was found to be warming across all layers (up to 0.3°C decade^{-1}) accompanied by salinification, except for localised cooling in the top 100 meters in the western basin, near the Fram Strait (-0.2°C decade^{-1}). This indicates additional heat uptake by the surface 0–100 meters and also increasing heat and salinity content of the AW inflow, while the transport of sea ice out of the AO has increased. The Amerasian Basin, on the other hand, showed a strong freshening trend culminating at the Beaufort Gyre. This is most likely due to the anticyclonic wind forcing and increasing freshwater inflow to the Beaufort Sea. The Amerasian Basin also showed a warming trend in the 300–700 m layers but a cooling trend in the 100–300 m layer north of the Chukchi Sea.

The ensemble approach worked well in dampening the extremities of singular ORAs, but some trends observed in the literature were missed due to disagreements between ORAs, especially in the Fram Strait and Beaufort Sea, which suggest that further improvements in both models and measurements are needed in those areas. Furthermore, improvements in deep ocean observations, how models handle the deeper ocean and assimilation methods are needed in order to study trends in the deeper depths in the AO. All in all, as the improvements come, the ORA MMM shows great potential for studies in the AO.

Avainsanat — Nyckelord — Keywords

Arctic Ocean, hydrography, salinity, temperature, reanalysis, modelling, climate change

Säilytyspaikka — Förvaringsställe — Where deposited

Kumpula campus library

Muita tietoja — Övriga uppgifter — Additional information

HELSINGIN YLIOPISTO — HELSINGFORS UNIVERSITET — UNIVERSITY OF HELSINKI

Tiedekunta — Fakultet — Faculty	Koulutusohjelma — Utbildningsprogram — Degree programme
Matemaattis-luonnontieteellinen tiedekunta	Ilmakehätieteiden maisteriohjelma Hydrosfäärin geofysiikka

Tekijä — Författare — Author

Laura I. S. Rautiainen

Työn nimi — Arbetets titel — Title

Havaitut muutokset Pohjoisen Jäämeren hydrografiassa

Työn laji — Arbetets art — Level	Aika — Datum — Month and year	Sivumäärä — Sidantal — Number of pages
Pro-gradu tutkielma	12.3.2020	72

Tiivistelmä — Referat — Abstract

Merten uusanalyysituotteista (ORA) saadaan tärkeää tietoa maailman merien tilasta. ORA:t eroavat toisistaan niiden erilaisten aineistolähteiden, merimallien, ilmastopakotteiden ja assimilaatiomenetelmien vuoksi. Näistä eroavaisuuksista huolimatta, parvi-menetelmää hyödyntämällä voidaan saavuttaa todenmukaisia merten keskitiloja. Voisiko merien uusanalyysituotteita hyödyntää myös muutosten tutkimisessa alueilla, joissa mittaukset ovat harvassa? Tässä tutkielmassa tulkitaankin muutoksia Pohjoisen Jäämeren hydrografiassa merten uusanalyysituotteiden avulla.

Tutkielmaa varten valittiin yksitoista merten uusanalyysituotetta: TOPAZ4, C-GLORS025v5, ECDA3, GECCO2, GLORYS2v4, GloSea5-GO5, MOVE-G2i, ORAP5, SODA3.3.1, UR025.4 ja ORAS5. EDCA3:a lukuunottamatta niistä muodostettiin monimalli-parvi (MMM). Data jaettiin syvyyden perusteella kerroksiin joiden keskiarvoistettua lämpötilaa ja suolaisuutta hyödynnettiin altaiden keskiarvoistettujen poikkeama-aikasarjojen ja trendien laskennassa. Poikkeama-aikasarjoja ja trendejä käytettiin muutostulkintaan tutkimusaikajakson aikana. Trendit laskettiin myös jokaista hilaa kohden, jotta ajallisten muutoksien lisäksi myös paikallisia muutoksia voitiin tutkia. Tuloksia vertailtiin havaintotuotteen EN4.2.0.g10 kanssa ja tilastollisia menetelmiä hyödynnettiin MMM-tuotteen tulkitsemisessa, jotta alueellisia heikkouksia ja vahvuuksia voitiin tunnistaa.

Euraasian altaan lämpötila ja suolaisuus kasvoi jokaisessa syvyyskerroksessa (maksimissaan 0.3 °C vuosikymmen^{-1}), lukuunottamatta paikallista viilenemistä 0–100 m syvyyskerroksessa altaan länsipuolella, Framinsalmen kohdalla (-0.2°C vuosikymmen^{-1}). Tämä johtunee pintakerroksen (0–100 m) lisääntyneestä lämpömäärästä sekä Atlantin veden suolaisuuden ja lämpömäärän kasvamisesta. Samanaikaisesti merijään ulosvirtaus Framinsalmen kautta on kiihtynyt. Ameraasian altaassa suolaisuus taas on kauttaaltaan vähentynyt keskittyen Beaufortin pyörteeseen johtuen antisyklonaalisista tuulipakotteesta ja kasvaneesta makean veden virtauksesta Beaufortinmerelle. Ameraasian allas myös lämpeni 300–700 m syvyyskerroksessa ja viileni 100–300 m syvyyskerroksessa Tŝuktŝimerestä hieman pohjoiseen.

Yksittäisten uusanalyysituotteiden erot tasottuivat hyvin parvi-meneltelmän avulla, mutta osa kirjallisuudessa havaituista muutoksista jäi uupumaan MMM-tuotteesta suurista eroista johtuen. Mittauksia ja mallinnusta tulisi kehittää erityisesti Framinsalmella ja Beaufortinmerellä. Lisäksi syvien merien mallinnuksessa, assimilaatiomenetelmissä ja mittauksissa tarvitaan kehitystä, jotta syvien merien muutoksia voitaisiin tulkita. Näiden kehitysten myötä MMM-tuotteesta tulee erittäin potentiaalinen meneltelmä Pohjoisen Jäämeren tutkimuksissa.

Avainsanat — Nyckelord — Keywords

Pohjoinen jäämeri, hydrografia, suolaisuus, lämpötila, uusanalyysi, mallinnus, ilmastonmuutos

Säilytyspaikka — Förvaringsställe — Where deposited

Kumpulan kampuskirjasto

Muita tietoja — Övriga uppgifter — Additional information

Contents

List of Figures

List of Tables

1. Introduction

1.1 The Arctic Ocean (AO)

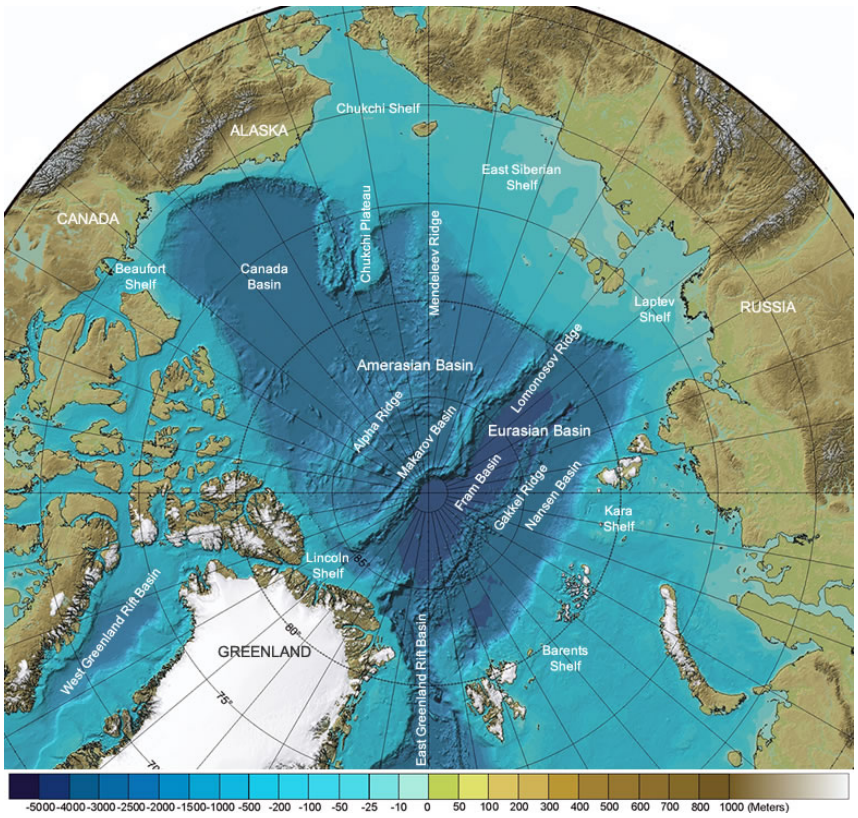

Figure 1.1: Bathymetry map of the AO showing the major basins and seas. Source: King (2017).

The Arctic is an ocean surrounding the North Pole limited in the south by two continents with connections to both the Atlantic via Greenland and Labrador Seas, and to the Pacific via Bering Strait (Figure 1.1). With the surface area of 9.4×10^6 km^2 and the average depth of 1038 m (Rudels, 2015), the Arctic Ocean (AO) is the smallest out of the five world oceans. Over half of its area is shallow shelf seas, the broad Eurasian marginal seas, namely the Barents Sea (200–300 m), the Kara Sea (50–100 m), the Laptev Sea ($<$ 50 m), the East Siberian Sea ($<$ 50 m) and the Chukchi Sea (50–100 m), and generally narrower shelves north of North America and Greenland (Rudels, 2009). The map

above (Figure 1.1) shows the bathymetry and the basins of the AO. The 500–850 m deep Greenland-Scotland Ridge separates the AO from the Northern Atlantic (Rudels, 2009). Furthermore, the Lomonosov Ridge divides the deep AO into two oceanic basins, the Amerasian Basin (3000 m deep) and the Eurasian Basin (3000–3500 m deep) with differing characteristics (Rudels, 2009). The Eurasian Basin is further divided into the Nansen and Amundsen basins by a mid-ocean ridge (the Gakkel Ridge), while the Amerasian Basin is separated by the Alpha Ridge and the Mendeleyev Ridge into the Makarov and the Canada Basins (Rudels, 2009, 2016).

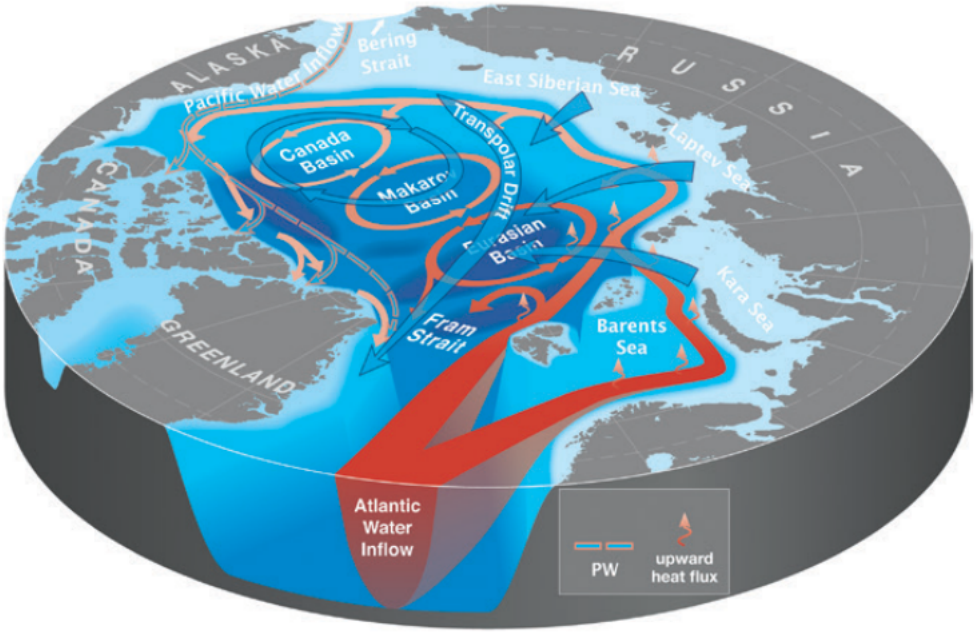

Figure 1.2: Schematic of the AO circulation. Source: Carmack et al. (2015).

1.1.1 The AO circulation

The circulation pattern of the AO is complex. As it is a semi-enclosed basin, the exchange of water is limited by, first of all, the continents, but also by water depth, as the only pathway allowing for two-way exchange is the 2600 km deep and 850 km wide Fram Strait (Rudels, 2015). In comparison, the only connection to the Pacific is the 50 m deep and 85 km wide Bering Strait (Rudels, 2015).

The wind and ice drift driven circulation of surface waters is anti-cyclonic in the Amerasian Basin due to the mean high pressure system above the Beaufort Sea, forming the Beaufort Gyre (Talley et al., 2011). In the Eurasian basin, the surface circulation is cyclonic (Talley et al., 2011). Convergence of the surface circulation patterns forms the Transpolar Drift which connects the two basins and flows toward the Fram Strait (Carmack et al., 2016). The freshwater input to the AO via the Canadian and Siberian

rivers (0.1 Sv, 1 Sv = 1×10^6 m^3s^{-1}), such as Ob, Yenisei, Lena and Mackenzie, and net precipitation (0.06 Sv) sustains a fresh and cold upper layer, Polar Mixed Layer (PML) (Woodgate, 2013; Rudels, 2009). The river inflow, and the relatively fresh Pacific inflow (0.8 Sv) at the Chukchi Sea, induce sea ice formation at the shelf seas and as a result, the salt-enriched shelf waters sink to form the Arctic halocline (AH) (Woodgate, 2013).

AH is a region of rapidly changing density between the lower salinity surface layer and the rest of the AO where both salinity and temperature increase with increasing depth (Polyakov et al., 2018). The top of the AH, 50 to 100 m in depth, is cold and in the lower part, from 100 m to 200 m, both temperature and salinity increase with depth (Polyakov et al., 2018). In the Amerasian basin the AH is stronger due to the inflow of relatively fresh Pacific Waters (PW) via the Bering Strait (Carmack et al., 2016). As the Atlantic and Pacific inflows are more saline than the surface waters, they sink, to a depth determined by their density, when they enter the AO. The warm and saline inflow from the Atlantic of about 7 Sv (Fahrbach et al., 2001) sinks to intermediate depth (150–800 m) and forms the Atlantic Water (AW) layer where salinity increases to 34.8 PSU (Carmack et al., 2016). The AW inflow creates the Arctic Ocean Boundary Current (AOBC) that flows cyclonically in the Eurasian Basin and along the Eurasian slope and Lomonosov Ridge (Woodgate, 2013). In the Amerasian Basin, the AW inflow is weaker and steered toward the Beaufort Sea (Woodgate, 2013). The Lomonosov Ridge splits the AOBC, half of which moves north along the ridge and the other half enters the Makarov Basin (Woodgate et al., 2001).

The warm PW sinks to 60–220 m depth and is generally confined to western AO (Carmack et al., 2016). The strong vertical stratification within the halocline inhibits the upward transport of heat. Below the halocline, intermediate and deep circulation are topography steered following the continental slope and mid-ocean ridges forming cyclonic gyres in both basins (as seen in Figure 1.2). Below the AW, around 900 m, lies the Arctic Bottom Water (ABW) that is colder than the AW (about 3°C) (Rudels, 2009). The ABW is composed of Arctic shelf water and Greenland Sea Deep Water (GSDW) (Talley et al., 2011). The GSDW forms via occasional deep convection within the Greenland Gyre (Talley et al., 2011). During winter, the temperatures cool and ice formation and vertical convection begin, eventually leading to the water being dense enough to sink below the warm saline water below, forming the ABW (Talley et al., 2011). The ABW contributes to the formation of Atlantic Deep Water overturning which is of vital importance to the global circulation and climate moderation (Somavilla, 2019).

1.1.2 The AO water masses

From the discussion in the section 1.1.1, the AO can be divided into five distinct water masses.

1. **PML**. Approximately 25 to 50 m thick layer with low salinity. Salinity is $\sim$ 30-32.5 PSU in the Amerasian basin and $\sim$ 32-34 PSU in the Eurasian Basin (Rudels, 2009). Salinity varies due to seasonal patterns of freezing and melting of sea ice (Talley et al., 2011).

2. **AH**. Approximately 100-250 m thick halocline where salinity increases with depth 32.5<S<34.5 PSU and temperature remains close to freezing (Rudels, 2009). The PML and AH together form the Arctic Surface Waters (ASW) (Talley et al., 2011).

3. **PW**. Lies at surface to 250 m in depth in the Amerasian Basin with temperatures above 2°C and S<33.0 PSU (Aksenov et al., 2016). At depths below 250 m, the PW gets heavily diluted (Aksenov et al., 2016).

4. **AW**. Approximately 400-700 m thick Atlantic Water layer with temperatures above 0°C and salinity from 34.5 to 34.8 PSU (Carmack et al., 2016; Woodgate, 2013).

5. **ABW**. Lies the deepest, salinity is $\sim$34.9 PSU and temperature in Eurasian Basin -0.97°C and in Amerasian Basin -0.55°C (Rudels, 2009).

1.2 Climate and sea ice

The AO is a subject to polar climate, which is characterised by persistent cold and relatively narrow annual temperature ranges. It also moderates the regional climate, even when covered by ice, as the warmer-than-air ocean releases heat to the atmosphere. Moreover, the ice coverage also contributes significantly to the global climate, as the higher albedo of snow and ice results in a cooling effect of the climate compared to the albedo of the bare ocean. The AO is partially covered by sea ice throughout the year with a seasonal pattern in its extent and thickness, with the minimum extent occurring in September ($\sim$5 Mkm^2) and the maximum extent around April ($\sim$15 Mkm^2) (Cottier et al., 2016). The ice coverage limits the transfer of heat, mass and momentum within the sea-atmosphere boundary layer and henceforth also dampens the surface waves (Woodgate, 2013). Recurrent latent heat polynyas in the Laptev, Barents and Kara Seas result in high production of sea ice that is pushed away by the wind and as such, the ice keeps forming readily in these "ice factories" (Talley et al., 2011). This results in constant brine rejection to the water body, making the shelf water dense enough to sink (Talley et al., 2011). Thus the

formation of sea ice plays an important role in the thermohaline driven circulation of the AO (Talley et al., 2011).

Sea ice processes, such as formation, melt, break-up and export, are regional and vary across the AO (Cottier et al., 2016). The newly formed ice drifts along the wind-driven surface currents (Cottier et al., 2016), the Beaufort Gyre (BG) in the Amerasian Basin and the Transpolar Drift that flows from the Siberian coast to the Fram Strait (see 1.2). The ice export out of the AO is approximately 0.09 Sv (Rudels, 2011).

1.2.1 Observed changes in sea ice and hydrography

Although remote and to some extent unreachable to humans, the Arctic still feels the consequences of the excessive GHG emissions as the intensified poleward heat transport advects more and more heat to the region and the complex feedback mechanisms, such as ocean-sea ice feedback system (Steiner et al., 2004), further amplify the regional warming. Indeed, the warming of the surface air has occurred at double the global rate, which is denoted as Arctic amplification. On top of ocean-sea ice feedback, other regional processes, such as increase in total water vapour content in the atmosphere, changes in cloudiness, relatively lower rate of heat loss to the atmosphere than that at sub-tropics and additional heat from newly formed sea ice, have also been proposed to be the cause of Arctic amplification (IPCC, 2019).

As a result, the changes are already observed in the Arctic. Namely the drastic changes in sea ice have been lifted as the flagship of climate change and for a reason, IPCC (2019) states that sea ice extent has decreased with strongest reductions in September, -12.8% per decade during 1979–2018, with coinciding thinning and shifting to overall younger ice. The observed changes are stronger during summer and lesser during winter with the summer trends being explained by sea ice loss in the East Siberian Sea and large declines in the Beaufort, Chukchi, Laptev and Kara Seas, whereas the winter trends are dominated by reductions in the Barents Sea (IPCC, 2019). The sea ice drift speed has also been observed to have increased and as a result, more ice is also transported out of the AO (IPCC, 2019). Furthermore, the AO could become virtually ice free within the next few decades (Holland et al., 2006; Overland and Wang, 2013).

Although changes in sea ice can be seen as the flagship of climate change, there is more than meets the eye as the consequences have also been felt in the hydrography of the AO. IPCC (2019) reports that the summer upper mixed layer temperature increased 0.5 °C per decade during 1982–2017 as a result of more solar heat being absorbed and stored by the surface layer as the sea ice extent decreased. Furthermore, also the AW total heat content has increased (Polyakov et al., 2017). Term "Atlantification" has been used to describe the observed changes in the Northern Barents Sea and Eurasian Basin as the

AH is weakening and also more heat is being advected to the northeast than previously (IPCC, 2019). In the PW, an increase of 0.5 °C has been observed between 2009–2013 and the integrated heat content has doubled over 1987–2017. Furthermore, 60% increase in the heat content of the inflow entering via Bering Strait has also been observed (IPCC, 2019).

On top of changes in heat content, changes have also been observed in the salinity of the AO. The changes in salinity are driven by the freshwater budget, mainly river runoff, net precipitation, sea ice and currents. IPCC (2019) reports a freshwater increase of $\sim$600 km^3 yr^{-1} with two-thirds contributing to decreases in salinity and one-third with thickening of the freshwater layer. Freshwater volume has increased in the Beaufort Gyre (by 40%) and decreased in the East Siberian, Laptev, Chukchi, Kara and Barents Seas (IPCC, 2019). The freshwater flux from rivers has increased while the inflow of freshwater through Bering Strait has also been observed to increase by $\sim$ 30 km^{3}yr^{-1} (IPCC, 2019). Increases in glacial discharges from the Greenland ice sheet have also been suggested (IPCC, 2019). Furthermore, the freshening is expected to continue as the river inflow is increasing due to intensifying hydrological cycle (IPCC, 2019).

All in all, the oceanic heat, salt and sea ice dynamics are intertwined. The transfer of heat is mainly from the warmer-than-air ocean to the atmosphere. Reductions in summer extent of sea ice allows for more short wave radiation to be absorbed by the ocean, while the upper ocean solar heating leads to thinner and overall younger ice that breaks easier under wind forcing. The diminishing sea ice extent also changes the planetary albedo, accelerating the global climate change due to ice-albedo feedback (Curry and Schramm, 1995). The ice-covered regions, such as the Arctic and northern North Atlantic, are significant regions for convection and formation of deep water (Griffies et al., 2009). The loss of perennial sea ice and increasing river inflow can lead to the freshening of the AO surface waters that in turn can cause to more freshwater being exported to the deep water formation sites, which can affect the global thermohaline circulation and as such, the global climate (Steiner et al., 2004).

1.3 Ocean reanalyses describe the state of the ocean

The ocean has a large inertia and is less subjectable to short-term climate variability than the other components of the climate system, and as such, can provide a clearer description of the long-term change (IPCC, 2013). Knowledge of the past and current states of the ocean are therefore important for acquiring information on the long term evolution of climate (IPCC, 2013). However, the observations are at times sparse and even non-existing, making the tracking difficult (IPCC, 2013). Especially in the AO, the harsh conditions for expeditions and perennial ice cover limit the studying of climate

change and development of ocean models. Ocean models use knowledge on physical processes to simulate ocean variability but they suffer from biases resulting from model formulation, specification of initial states and forcing (Balmaseda et al., 2015). Ocean reanalyses (ORAs) combine an ocean model, atmospheric forcing and observations using a data assimilation method in order to give a description of the state of the ocean that can be more accurate than model- or observation-only products (Balmaseda et al., 2015; Uotila et al., 2018).

Many research and operational institutes have created their own ORAs to study the past states of the ocean and to initialise seasonal forecasts (Palmer et al., 2017). ORAs are also used to reduce instrumental biases in time series data, that occur, for example, when an instrument is replaced by another instrument. New versions of existing ORAs are published every once in a while as the methods are revisited and improved (Palmer et al., 2017). For example, the period from 1990s to 2000s is often known as the "Argo revolution" as the deployment of Argo floats allowed for the detection of hydrographical features, temperature, conductivity (salinity), pressure (depth) and currents, in real time (Destin, 2014). The change is seen in long term ORAs where a drastic change in trends of temperature and salinity can be observed in early 2000s (Palmer et al., 2017). Before the Argo revolution, reasonable ocean coverage was only achieved for the upper couple of hundred meters, starting from the 1960s and hence, some of the long running historical estimates of hydrography are limited to the upper 700 meters (Palmer et al., 2017).

The Ocean Reanalyses Intercomparison Project (ORA-IP) and its polar counterpart, Polar Ocean Reanalyses Intercomparison Project (PORA-IP) have studied the representativeness of ORAs, and the ensemble average in particular, in describing various ocean variables, for example sea level, ocean heat and salt content and sea ice (Balmaseda et al., 2015; Uotila et al., 2018). Uotila et al. (2018) found the ensemble mean to be a useful product, if its restrictions are acknowledged, as the deviations from observations are smaller than for individual ORAs and as such, the ensemble mean can be used to acquire knowledge on the physical state of the AO. Their study focused on the representativeness of the mean state of the ocean which led to this thesis as a continuation study where the observed changes in ORAs, regarding temperature and salinity, are examined. Such study has not been previously carried out.

1.4 The goals and outline of the thesis

This thesis aims to address the question if the Arctic Ocean has significantly changed, in terms of temperature and salinity, in the previous decades. To achieve this goal 11 ORAs, TOPAZ4, C-GLORS025v5, ECDA3, GECCO2, GLORYS2v4, GloSea5-GO5, MOVE-G2i, ORAP5, SODA3.3.1, UR025.4 and ORAS5, were chosen and ensemble mean (MMM) was

formulated based on these ORAs, excluding ECDA3. Using such a comprehensive, unique, multi-model data set to analyse observed changes in the hydrography of the AO has not been previously performed. This thesis also aims to answer the question if the ensemble approach is a robust method for change analysis in the AO. Hence, the robustness of the ORAs and MMM for change analysis is also assessed along the uncertainties of the results. Although no absolute truth to compare the results of this thesis to exists, the ensemble mean trends are compared to a observational product, EN4.2.0.g10, that overlaps the study period from 1993–2010. Also standard deviation and the ensemble spread (Shi et al., 2017), are used to evaluate areas of noise and uncertainty in the trends. Lastly, the thesis aims to provide some analogue to the results in the context of known dynamics and literature.

Background to this thesis was provided in Chapter 1, Introduction. It presents the main characteristics of the AO in terms of water masses and circulation, reviews reported changes in the hydrography and sea ice of the AO and also introduces ORAs as a viable method for trend detection. Chapter 2, Theory, of this thesis presents, not exhaustively, the physics that determine the dynamics of the hydrography relevant to the AO. Chapter 3, Materials and Methods, presents the ORA products used in this study and also the methods that are used for trend detection and validation. In Chapter 4, the results of this thesis are presented and illustrated. Chapter 5 provides analogue to the results and Chapter 6 has concluding remarks of the thesis and provides some future reflections.

2. Theory

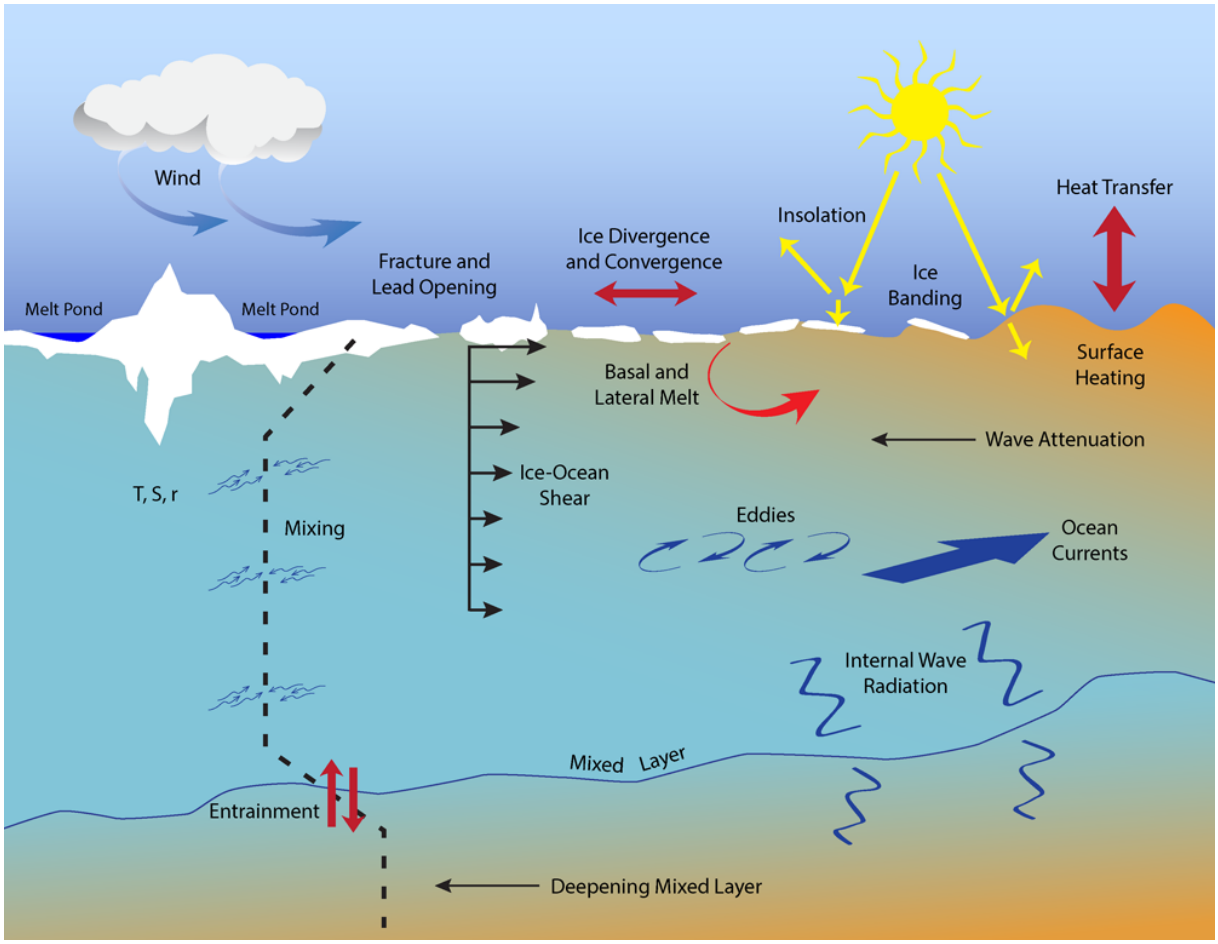

Figure 2.1: Key processes affecting hydrography of the Arctic Ocean. Source: Lee et al. (2012).

This chapter aims, by no means exhaustively, to present the main processes determining the hydrography, in terms of temperature and salinity, in the AO while reflecting on the choices ocean models have in representing them. Ocean models, in general, aim to depict the time-dependent three-dimensional flow of a fluid by solving non-linear Navier-Stokes equations (Kantha and Clayson, 2000). These partial differential equations are supplemented by conservation of scalar properties, such as potential temperature and salinity (Kantha and Clayson, 2000). Salinity denotes the concentration of salt in the water $[\frac{g}{kg}]$ and the Practical Salinity Unit (PSU) is used in this thesis to express salinity.

The main processes affecting the hydrography of the AO that are discussed in this chapter can be seen in Figure 2.1. The surface hydrography is affected by surface heat flux, precipitation, evaporation, river inflow and sea ice processes. In the AO interior, processes, such as internal waves and currents, mix heat and salt both laterally and vertically. Close to the bottom, the topography, tides and the bottom shear induce mixing. Accordingly, this chapter is divided into two sections, surface and interior, to describe the processes related to the hydrography of each part of the AO. Vectors are denoted in bold.

2.1 Surface processes

The surface processes shape the hydrography of the PML. In ocean models, the surface processes are accounted in as boundary conditions, including the surface wind stresses (τ), surface heat flux (Q_{ao}), surface freshwater flux and sea ice salt flux (Brodeau et al., 2009). The resulting fluxes of heat, salt and freshwater are calculated from gridded weather reanalysis products using bulk formulas (Brodeau et al., 2009). Common bulk formulas include, for example, the CORE and the CLIO bulk formulae. In this section, examples are drawn from the CORE bulk formulae described in Large and Yeager (2004).

2.1.1 Heat budget

The amount of energy (ΔH) needed to heat a certain mass of water by a change in temperature (ΔT) can be calculated:

$$\Delta H = c_p m \Delta T \quad [J] \tag{2.1}$$

where c_p is the specific heat capacity of water [J kg^{-1} °C^{-1}] and m the mass [kg]. Due to the high heat capacity of water, the upper layer of the ocean acts as a heat storage and as such, is very important in regulating the regional climate (Goosse et al., 1999). Indeed, the upper 60 m of the AO absorbs 99.8 % of the incoming solar energy (Steele et al., 2010).

The change of heat content is determined by the heat fluxes between the atmosphere and the ocean, and the sea ice and the ocean. Figure 2.2 depicts the heat balance in the presence of ice. In the AO, the surface heat flux can occur via thin sea ice, open sea and leads. Formation of snow cover on top of sea ice further insulates the AO due to the low thermal conductivity of snow, and affects the reflectivity of the surface as the albedo of snow is ∼0.85 compared to 0.4–0.7 of bare ice (Carmack et al., 2015).

In CORE bulk formulae, a fraction of the grid point can be covered by ice f_i, which leaves a fraction $f_o = 1 - f_i$ open for the atmosphere (Large and Yeager, 2004). And the

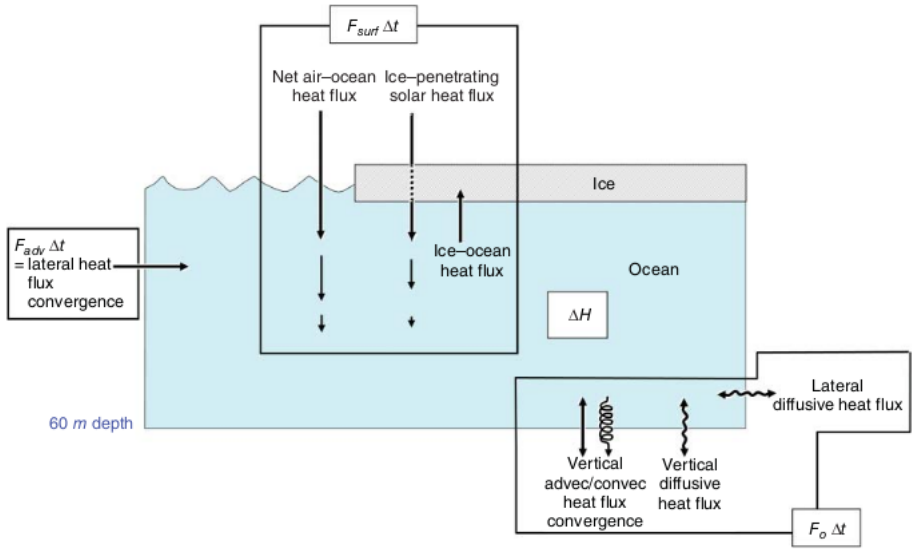

Figure 2.2: Heat balance in ice covered oceans. Source: Cottier et al. (2016).

heat budget can be expressed as:

$$Q_a = f_i Q_{io} + f_o Q_{ao} \tag{2.2}$$

and surface stress:

$$\boldsymbol{\tau} = f_i \boldsymbol{\tau_{io}} + f_o \boldsymbol{\tau_{ao}}, \tag{2.3}$$

where "ao" and "io" denote air-ocean and ice-ocean fluxes (Large and Yeager, 2004). The air-ocean heat flux:

$$Q_{ao} = Q_{SW} + Q_{LW} + Q_S + Q_H + Q_P + F_o \tag{2.4}$$

where Q_{SW} is the net shortwave radiation, Q_{LW} the net longwave radiation, Q_S the sensible heat flux, Q_H the latent heat flux, F_o the advected and diffused ocean heat fluxes and Q_p the snow-precipitation heat flux (Steward, 2008; Large and Yeager, 2004). The net shortwave radiation varies depending on the time of the day and season, and before it reaches the surface, atmosphere absorbs, reflects and scatters a part of it, making cloudiness an important factor. Albedo of the surface determines how much of the shortwave radiation is reflected back to the atmosphere, and how much is absorbed by the surface. Part of the shortwave radiation is also transmitted to the water body via ice. Q_{LW} is generally negative throughout the year but Q_{SW} accounts for the bulk of the warming during summer (Persson and Vihma, 2016). Furthermore, the advective heat flux resulting from lateral gradients of heat content, can be large in the presence of warm currents. In Figure 2.2, the ocean heat fluxes (F_o) result from vertical advection and diffusion, vertical heat

flux convergence and vertical convection. For the AO, the main sources of advected heat include the inflows from the Atlantic, Pacific and rivers.

Turbulence produces chaotic, rapid variations in velocity which produce turbulent fluxes where the mean velocity is accompanied by fluctuations of temperature and/or humidity (Hartmann, 2016). Measuring these turbulent fluxes accurately requires measurements of velocity, humidity and temperature which above the AO are not feasible to be routinely taken and due to the rapid, small scale fluctuations, they are not simulated by global models (Hartmann, 2016). Instead, bulk formulas are commonly used:

$$Q_S = \rho_a c_p \overline{w'\theta'} = \rho_a c_p C_H(\theta(z_\theta) - \theta(SST)) \mid \Delta\mathbf{U} \mid \tag{2.5}$$

$$Q_H = \rho_a L_E \overline{w'q'_a} = \rho_a L_E C_E(q(z_q) - q_{sat}(SST)) \mid \Delta\mathbf{U} \mid \tag{2.6}$$

$$\tau = \rho_a C_D \mid \Delta\mathbf{U} \mid \Delta\mathbf{U} \tag{2.7}$$

where ρ_a is the density of air, c_p is the heat capacity of air, w' is the fluctuation of the vertical velocity, θ' is the fluctuation of potential temperature, L_E is the latent heat of evaporation, q(z_q) specific humidity at height z_q, $\theta(z_\theta)$ potential air temperature at height z_θ, $\mid \Delta\ \mathbf{U} \mid = \mid \mathbf{U}(z_u) - \mathbf{U}_0 \mid$ is the vector difference between wind at height z_u and the surface current and C_E, C_H and C_D are transfer coefficients for evaporation and sensible heat and the drag coefficient, respectively (Large and Yeager, 2004). Although latent and sensible heat fluxes are small, heat is vented out effectively via leads ($Q_S + Q_H$ up to hundreds Wm^{-2}) and results in local convection (Persson and Vihma, 2016), making the percent of open water an important factor regarding determining the heat budget for the AO.

Snow-precipitation also leads into a heat flux, Q_P:

$$Q_P = -L_f P_s, \tag{2.8}$$

where L_f is the latent heat of fusion and P_s snow precipitation. Q_P is negative as when the snow melts in the ocean, the ocean loses energy.

The sea ice processes are also tied in to the heat balance of the surface layer. The CORE bulk formula assumes that the ocean gains heat and salt in ice formation and loses heat when ice melts (Large and Yeager, 2004). The resulting fluxes:

$$Q_{io} = Q_M + Q_F + Q_B + Q_{PS} \tag{2.9}$$

The heat flux to the ocean through thin ice (Q_{PS}) can be limited due to high albedo of the snow cover or thickness of ice (Large and Yeager, 2004). When sea-ice and/or snow are melting, cooling melt flux $Q_M < 0$ (Large and Yeager, 2004). When frazil ice forms, $Q_F > 0$ keeps the ocean at the freezing temperature and most of the salt is rejected to the ocean. Heat flux associated with the formation of basal ice, Q_B, is usually close to zero due to the latent heat of fusion balancing the basal cooling (Large and Yeager, 2004).

2.1.2 Freshwater budget

The AO only contains 1% of world ocean's seawater but receives 11% of the world's river inflow (Lammers et al., 2001). The AO also has a positive net precipitation, seasonal ice melt and the inflow from the Pacific that is relatively fresh, making the freshwater input per unit area the greatest compared to the rest of the world ocean (Nummelin et al., 2015). The freshwater flux in CORE bulk formulae:

$$F = f_i F_{io} + f_o F_{ao} + R, \tag{2.10}$$

where F_{io} is the ice-ocean freshwater flux, F_{ao} is atmosphere-ocean freshwater flux and R is the runoff from rivers (Large and Yeager, 2004). The atmosphere-sea freshwater flux:

$$F_{ao} = P + E, \tag{2.11}$$

where P is the precipitation and E evaporation (Large and Yeager, 2004). Measuring marine precipitation accurately is difficult due to lack of *in-situ* data and as such, the accuracy of the data is uncertain (Large and Yeager, 2004). In CORE bulk formulae, precipitation is calculated as water if the corresponding surface air temperature is greater than the freezing temperature of freshwater (0°C) and as snow if below it (Large and Yeager, 2004).

The seasonal melting of sea ice leads to input of freshwater on the top layer which under ice is kept at near freezing temperatures limiting evaporation (Rudels, 2016) and restratifies the water column. Freezing, on the other hand, releases brine to the water column enriching the surface waters with salt, causing the top layer to become unstable leading to convection (Cottier et al., 2016). The ice-ocean freshwater flux:

$$F_{io} = F_M + F_F + F_B, \tag{2.12}$$

where F_F is the freshwater flux that is negative during the formation of frazil ice, F_B is the freshwater flux that is negative during the formation of basal ice and lastly the ice melt water flux, F_M, that is positive during sea-ice and snow melt (Large and Yeager, 2004). To quantify these fluxes, it is important to determine how much salt is kept in ice, and rejected from ice. The bulk salinity of sea ice:

$$\frac{S_i}{S_0} = \frac{\rho_o}{\rho_i}\phi_c(1 + \frac{h}{z_x}) \tag{2.13}$$

where S_0 is the salinity of the sea water and ϕ_c is a critical ice porosity limiting desalination and $\frac{h}{z_x}$ is the dimensionless thickness of the desalinating layer (Petrich and Eicken, 2016). The bulk salinity method is a parametrisation based on the analytical solution of the mass conservation of gravity-driven fluid motion in sea ice that assumes a constant growth rate

and a simplified permeability profile (Petrich and Eicken, 2016). Over time, desalination decreases the amount of salt hold by the ice via processes of gravity drainage and meltwater flushing (Notz and Worster, 2009).

The salinity of the AO is not evenly distributed with the highest salinities of about 35 PSU occurring at the AW inflow and lowest of about 0 PSU at river mouths (Carmack et al., 2016). The pathways of Eurasian river inflow varies with the Arctic Oscillation as it has an effect on the Transpolar Drift and the Ekman convergence intensity in the Beaufort Gyre (Nummelin et al., 2015). With a high Arctic Oscillation index, the inflow is transported to the Canada basin, whereas with a low index, the inflow is toward the Fram Strait (Nummelin et al., 2015). Furthermore, the atmospheric forcing also causes alternating modes in the PML of stronger and weaker anti-cyclonic circulation over the Canada Basin with the weaker mode associated with stronger cyclonic circulation over the shelf seas and the Eurasian side (Pemberton et al., 2016). During the stronger mode, FW is collected and accumulated in the Beaufort Gyre and in turn released and pushed toward the Canadian Archipelago during a weaker mode (Pemberton et al., 2016). This distribution of salinity plays a major effect on the circulation and mixing in the AO (Carmack et al., 2016).

2.1.3 Restoring surface salinity and temperature

In ocean models, Q_{io} and F_{io} can also be estimated by:

$$Q_{io} = C_Q(SST_o - T_1) \tag{2.14}$$

$$F_{io} = C_F(S_1 - SSS_o) \tag{2.15}$$

where SST_o and SSS_o are the observed sea surface temperature and salinity, and T_1 and S_1 the model prognostic temperature and salinity of the upper model layer (Large and Yeager, 2004). The restoring coefficient C_Q and C_F are used to restore the model surface temperature and salinity toward observations on a desired time scale (Large and Yeager, 2004). Without restoring, long-running model SST and SSS can drift too far from the observations and become erroneous (Griffies et al., 2009). Hence, restoring is used in ocean-only models to limit the errors in the model simulated surface properties (Griffies et al., 2009). However, Griffies et al. (2009) claim that in ice-covered regions, it is perhaps not justified to apply restoring and no analogue has yet been established.

2.2 Below the surface

Once the boundary conditions have been established, a response within the ocean occurs. As potential temperature and salinity are conservative scalars, mixing and advection

accounts for the redistribution of the heat and salt both laterally and vertically within the AO. Mixing in the near surface boundary layer is largely driven by forcing conditions while in the ocean interior tracers are transported by large-scale currents and mesoscale eddies. The wind-driven turbulence is reduced in the AO due to vertical stratification and presence of sea ice (Rudels et al., 2009). This makes other mixing processes more important, such as internal waves, shear instabilities, inertial oscillations, tides, double diffusion and bottom boundary layer (Large et al., 1994; Rudels et al., 2009). In this section, the primitive equations governing the dynamics and their assumptions and parametrisations are discussed.

2.2.1 The primitive equations

Changes in salinity, temperature and/or pressure result in changes in the water body. Together, they determine the density of a water parcel. In the AO where the temperature ranges are narrow, salinity plays a significant role in determining the density of the seawater and therefore affects the circulation and mixing (Carmack et al., 2016). In order to determine the movement of water, accurate measurements of density are needed (Steward, 2008). However, density is rarely measured but calculated using the equation of state (Steward, 2008). Accordingly, the equation of the state of seawater is a function of salinity (S), temperature (T) and pressure (p):

$$\rho = \rho(T, S, p) \tag{2.16}$$

TEOS-10 is the current version on determining density of seawater but the International Equation of State (1980) is still widely used. See IOC et al. (2010) for details.
Using conservation of mass, information about flows in the ocean can be deduced. In the Eulerian frame of reference, the conservation of mass:

$$\frac{\partial \rho}{\partial t} + \nabla \cdot (\rho \boldsymbol{v}) = 0, \tag{2.17}$$

where $\boldsymbol{v}$ is the velocity vector. Important forces setting fluid on motion are pressure gradients, gravity and friction. We can write the forces to equal the total derivative of the velocity vector:

$$\frac{D\boldsymbol{v}}{Dt} = -\frac{1}{\rho}\nabla p - 2\Omega \times \boldsymbol{v} + \boldsymbol{g} + \boldsymbol{F_r}, \tag{2.18}$$

where $\mathbf{g}$ is the acceleration due to gravity, $\mathbf{F_r}$ friction and $\mathbf{\Omega}$ the rotation rate of the Earth and $\frac{1}{\rho}\nabla p$ is the pressure term (Steward, 2008). Coriolis force ($2\mathbf{\Omega} \times \mathbf{v}$) is a function of latitude and the rotational effects are stronger in the polar seas. Writing the total derivative ($D_t\ \boldsymbol{v}$) open and writing the terms in Cartesian coordinates, we achieve the

momentum equation:

$$\frac{\partial u}{\partial t} + u\frac{\partial u}{\partial x} + v\frac{\partial u}{\partial y} + w\frac{\partial u}{\partial z} = -\frac{1}{\rho}\frac{\partial p}{\partial x} + 2\Omega v \sin\theta + \nu_m \nabla^2 u, \tag{2.19}$$

$$\frac{\partial v}{\partial t} + u\frac{\partial v}{\partial x} + v\frac{\partial v}{\partial y} + w\frac{\partial v}{\partial z} = -\frac{1}{\rho}\frac{\partial p}{\partial y} - 2\Omega u \sin\theta + \nu_m \nabla^2 v, \tag{2.20}$$

$$\frac{\partial w}{\partial t} + u\frac{\partial w}{\partial x} + v\frac{\partial w}{\partial y} + w\frac{\partial w}{\partial z} = -\frac{1}{\rho}\frac{\partial p}{\partial y} + 2\Omega u \cos\theta - g + \nu_m \nabla^2 w, \tag{2.21}$$

where ν_m is the kinematic molecular viscosity and θ the latitude (Steward, 2008). Lastly, the key equations also include conservation of enthalpy (temperature):

$$\frac{\partial T}{\partial t} + (\mathbf{u} \cdot \nabla)T - \kappa_T \nabla^2 T = \frac{1}{\rho c_p} S_{heat}, \tag{2.22}$$

where c_p is the specific heat at constant pressure, $\boldsymbol{u} \cdot \nabla T$ the advection of heat, $K\ \nabla^2\ T$ diffusion of heat and S_{heat} the source term (McPhee, 2008). The corresponding equation for salt:

$$\frac{\partial S}{\partial t} + (\mathbf{u} \cdot \nabla)S - \kappa_S \nabla^2 S = \frac{1}{\rho} S_{salt} \tag{2.23}$$

where S is salinity and S_{salt} the source term (McPhee, 2008).

The above presented equations are too computationally demanding to be solved at a global scale while maintaining fine-enough resolution in time and space to still accurately represent processes affecting the state of the ocean. Hence, assumptions are made to simplify the equations (Griffies, 2004). In the world ocean, variations in density (ρ) are relatively small (2.5% of the average density ρ_o) (Mellor and Ezer, 1995) and hence have no effect on inertia. Thus in ocean models, it is common to ignore the density variations in momentum equations unless tied to gravitational buoyancy force (acceleration due to gravity) (Mellor and Ezer, 1995). This is known as the Boussinesq approximation. When the vertical scale of motion is small compared with vertical scales of density variations, such as in most of the world ocean, the Boussinesq approximation is a valid approximation (Mellor and Ezer, 1995). Even so, the fluid flow is often assumed to be incompressible and the resulting continuity equation is:

$$\nabla \cdot \mathbf{v} = 0 \tag{2.24}$$

$$\frac{\partial u}{\partial x} + \frac{\partial v}{\partial y} + \frac{\partial w}{\partial z} = 0 \tag{2.25}$$

This indicates that volume, rather than mass, is being conserved and any change in volume only occurs when volume is either added or removed. Therefore the Boussinesq

approximation eliminates the changes in steric sea level (Griffies, 2004). The model can however be adjusted to the steric effects (Mellor and Ezer, 1995).

Ocean models can be divided into hydrostatic, non-hydrostatic or quasi-hydrostatic depending on how they treat the derivative of the vertical momentum. When the vertical scale is much smaller than the horizontal scale, h/L << 1, the total derivative of the momentum can be assumed to be much smaller than the buoyancy term (i.e. contains far less energy) and the vertical pressure gradient becomes the product of density and the gravitational acceleration:

$$\frac{\partial p}{\partial z} = -\rho g \tag{2.26}$$

The hydrostatic approximation essentially concludes that the pressure at a point is determined by the weight of the fluid above it (hydrostatic pressure) which makes the description of the pressure field, and therefore the geostrophic currents, easier (Griffies, 2004; Fox-Kemper et al., 2019). As a consequence, strong vertical momentum in convective regions, such as in parts of the AO, needs to be parametrised (Griffies, 2004).

The ocean, as most natural flows, is turbulent in nature. Hence, the primitive equations of motion and conservation are Reynolds averaged (see for example Cushman-Roisin, 1994), which leads to addition of Reynolds stress terms, here expressed as the additional forces per unit mass in x-direction of the momentum equation:

$$F_x = -\partial_x\langle u'u'\rangle - \partial_y\langle u'v'\rangle - \partial_z\langle u'w'\rangle \tag{2.27}$$

The Reynolds stress terms in x-direction, transfer eastward momentum ($\rho\ u$) in x, y and z directions (Steward, 2008). For example, the new term $\rho(u'w')$ depicts the downward transport of eastward momentum (Steward, 2008). Following the K-theory, these stresses are parametrised using the Eddy viscosities (K: horizontal, ν: vertical):

$$\partial_x\langle u'u'\rangle = 2K\frac{d\langle u\rangle}{dx}, \tag{2.28}$$

$$\partial_y\langle u'v'\rangle = K(\frac{d\langle v\rangle}{dx} + \frac{d\langle u\rangle}{dy}), \tag{2.29}$$

$$\partial_z\langle u'w'\rangle = \nu\frac{d\langle u\rangle}{dz} + K\frac{d\langle w\rangle}{dx} \tag{2.30}$$

and the momentum equation in x- and y directions (2.19, 2.20) can now be written including these parametrisised Reynolds stress terms:

$$\frac{\partial u}{\partial t} + u\frac{\partial u}{\partial x} + v\frac{\partial u}{\partial y} + w\frac{\partial u}{\partial z} - fv = -\frac{1}{\rho}\frac{\partial p}{\partial x} + \frac{\partial}{\partial x}(K\frac{\partial u}{\partial x}) + \frac{\partial}{\partial y}(K\frac{\partial u}{\partial y}) + \frac{\partial}{\partial z}(\nu\frac{\partial u}{\partial z}) \tag{2.31}$$

$$\frac{\partial v}{\partial t} + u\frac{\partial v}{\partial x} + v\frac{\partial v}{\partial y} + w\frac{\partial v}{\partial z} + fu = -\frac{1}{\rho}\frac{\partial p}{\partial y} + \frac{\partial}{\partial x}(K\frac{\partial v}{\partial x}) + \frac{\partial}{\partial y}(K\frac{\partial v}{\partial y}) + \frac{\partial}{\partial z}(\nu\frac{\partial v}{\partial z}) \quad (2.32)$$

Turbulent flow regime gives rise to eddies that transport anomalously warm or cold water effectively, leading to mixing. Essentially, the vertical displacement works against buoyancy force and a simple equation for vertical mixing of T/S by eddies can be given as:

$$\frac{\partial X}{\partial t} + w\frac{\partial X}{\partial z} = \frac{\partial}{\partial z}(K_z\frac{\partial X}{\partial z}) + S_X, \quad (2.33)$$

where X is either temperature or salinity, K_z ($\mathrm{m^2\ s^{-1}}$) is the vertical eddy diffusivity, w is Reynold's averaged vertical velocity and S_X the source term (Steward, 2008).

The turbulent eddies come in various ranges, from centimeters to hundreds of kilometers in diameter and from seconds to years in time. Eddies with a diameter greater than 10 km that persist longer than a day, are known as mesoscale eddies. Other mesoscale processes include large-scale gyres, boundary currents and meanders (Nurser and Bacon, 2014).

2.2.2 Scales of motion

The resolution needed to describe mesoscale processes can be estimated using internal Rossby radius of deformation (R_o). Nth R_o is the length scale at which rotation effects become as important as buoyancy:

$$R_{o,n} = \frac{NH}{n\pi f} \quad (2.34)$$

where N = Brunt-Väisälä buoyancy frequency, H is the depth, $f = 2\Omega \sin\phi$ the Coriolis parameter and n number of internal modes (Nurser and Bacon, 2014). As the Coriolis parameter is a function of latitude (ϕ), the Rossby radius at the AO is small, from 5 km in the Nansen Basin to 15 km in central Canadian Basin (Nurser and Bacon, 2014). In the shelf regions, the internal Rossby radius is even smaller, around 1–7 km, due to weak stratification and shallow water (Nurser and Bacon, 2014). The resolution of the model determines how fine the model can solve eddies. For the model to be eddy-solving, minimum of four grid points per the eddy diameter is needed and two grid points to be eddy-permitting (Nurser and Bacon, 2014).

Accurate presentation of the eddying features poses one of the biggest challenges in ocean modelling as mesoscale eddies contain more energy than the time averaged ocean currents and hence affect large-scale processes, such as heat uptake (Uotila et al., 2005). The primitive equations used in models are solved at a large scale defined by the specified grid spacing and time step of the model in question and if the model is eddy-solving, the lateral mesoscale turbulence can be solved (Griffies et al., 2000). As mentioned, the

Reynolds's decomposition gives rise to the Reynolds stress terms which leave the Navier-Stokes equations unclosed. To close the equations, the smaller than-grid-size processes must be presented at a grid-size scale (Griffies et al., 2000). The parametrisations of sub-mesoscale processes include statistical turbulence closures and empirical closures (Griffies et al., 2000).

2.2.3 Parametrisation of vertical turbulence

One of the most common vertical mixing parametrisation is derived from K-theory, where turbulent fluxes are related to the local gradients of large-scale quantities by eddy diffusivity and viscosity coefficients (K) (Griffies et al., 2000). Some models present K as a function of gradient Richardson number while others use the Mellor and Yamada (MY) approach (Griffies et al., 2000). In the MY approach, prognostic equations are used to solve turbulence fields and to compute the turbulent length and velocity scales which are then used to calculate the vertical diffusivity and viscosity (Griffies et al., 2000). One of the most common parametrisations is the K-Profile Parametrisation (KPP), where, for example, the vertical transfer of heat:

$$\frac{\partial T}{\partial t} = \partial_z(K_z \partial_z T - \gamma) \tag{2.35}$$

where K_z is the vertical diffusivity, $\partial_z = \frac{\partial}{\partial_z}$ and γ a non-local transport term (Griffies et al., 2000). The KPP parametrisation is used for example in MIT, HYCOM and NEMO ocean models.

2.2.4 Vertical mixing

The stability of a water column indicates the stability of the vertical stratification and can be quantified with the density gradient, E:

$$E = -\frac{1}{\rho}\frac{\partial \rho}{\partial z} \tag{2.36}$$

If $E > 0$ the water column is stable, $E = 0$ the water column is neutral and if $E < 0$ the water column is unstable. Momentary static instabilities are possible but the resulting processes will rapidly stabilise the water column. In the AO, melting of sea ice has a stabilising effect on the vertical stratification as less dense water is released at the top of the water body, whereas freezing of sea ice introduces instability with the brine injection increasing the density at the ice-ocean boundary layer. The increasing density results in immediate vertical advection, referred to as convection, of the denser water, until more dense water is contacted at depth.

For example, shelf water formation drives the water-mass formation and modification in the AO (Rainville et al., 2011). When relatively fresh shelf waters freeze rejecting some

of the salt in the process, the surface waters to become enriched with salt and increased in density, causing them to sink to a depth limited by the AH (Figure 2.3). The salty cold waters form the top part of the AH and spread to the interior (Rainville et al., 2011).

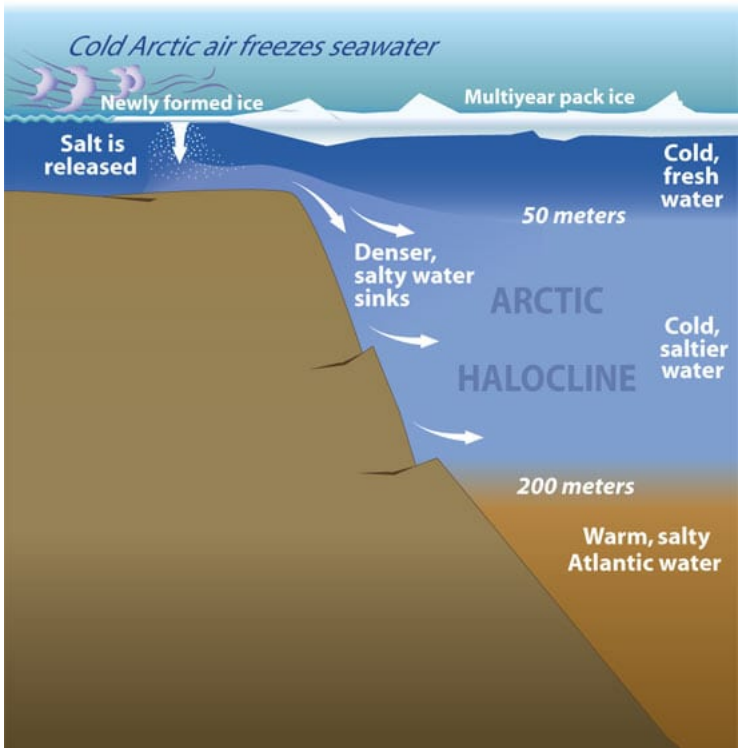

Figure 2.3: The formation of the Arctic Halocline. Source: Doucette (2018).

The influence of stability on stratification of a water layer can be defined using Brunt-Väisälä buoyancy frequency:

$$N^2 = -\frac{g}{\rho_o}\frac{\partial \rho}{\partial z} \tag{2.37}$$

where g is acceleration due to gravity, ρ_o is the reference density and ρ is potential density (Steward, 2008). It gives the maximum frequency of the internal waves. Brunt-Väisälä buoyancy frequency is used in ocean models to determine ocean stratification for parametrisation of mixing processes, for example, in vertical diffusion (Madec et al., 2017).

Sea ice cover acts as a barrier to transfer of momentum between atmosphere and the ocean. As such it dampens the wind generated surface waves and internal waves, leading to smaller upper ocean variability (Rainville et al., 2011). However, as the summer sea ice extent is diminishing, wind forcing will have an increasing effect in the AO (Rainville et al., 2011). In the AO, the waves are largest during summer when the sea ice extent is the lowest and in early winter due to strong winds (Dosser et al., 2013). Wind forcing over open water or on sea ice generates near-inertial waves in the AO which results to inertial

currents in the mixed layer (Dosser et al., 2013). The horizontal variations in velocity in turn cause convergence and divergence in the mixed layer which drive internal waves (Dosser et al., 2013). However, observations show that the mixing via internal waves is minimal at the central AO (Rainville et al., 2011). Figure 2.4 shows the mixing processes responsible for most of the variation for both the ice covered AO and a possible future scenario, where the wind forcing has become more important, causing surface waves and internal wave fields to be stronger.

As mixing via waves and internal waves is limited, other processes become more important, such as molecular diffusion (Rainville et al., 2011). The AO is strongly stratified with relatively fresh and cold PML on top, warm and saline AW in the middle, and cold and saline ADW at the bottom. Perturbation at the boundaries of these layers, can lead to mixing via diffusion. As the coefficient for molecular heat diffusion κ_T is hundredfold compared to the molecular diffusion coefficient for salinity κ_S, the diffusion of heat and salt occur at different paces resulting in phenomena known as double diffusion, where the potential energy from the unstably stratified component is released and used for mixing (Rudels et al., 2009). Double diffusive convection has two modes, the saltfinger mode and diffusive convection mode (Rudels et al., 2009). In a stable situation where warmer saline water is on top of colder fresher water, a parcel displaced downward would reach a thermal equilibrium with its surroundings while remaining more saline (Rudels et al., 2009). Thus the now cold but saline water parcel would continue sinking, creating a saltfinger (Rudels et al., 2009). In the AO, double diffusion is in the form of diffusive convection, as the surface waters are cold and fresh and lie on top of warm and saline water. When displaced downward, a water parcel absorbs heat from the warmer surroundings via diffusion and consequently becomes lighter and moves upward, creating an oscillatory instability (Rudels et al., 2009). This can be observed as sequences of well-mixed layers with abrupt density changes occuring in thin interfaces (Merryfield et al., 1999). The rates of double-diffusive mixing can be determined using buoyancy ratio:

$$R_\rho = \frac{\alpha \partial_z T}{\beta \partial_z S} \tag{2.38}$$

where α is the coefficient of thermal expansion and β the coefficient of saline contraction (Bourgain and Gascard, 2011). When R_ρ increases, the heat diffusion increases in relation to salt diffusion, and if $R_\rho = 1$, there is no double diffusion. Although the AW heat is trapped below the AH, diffusive convection has been suggested as one of the mechanisms that could transfer heat upwards and be a part of the reason why sea ice extent and thickness are decreasing. Polyakov et al. (2017) approximated this transfer to be from 0.3 Wm^{-2} in the central Amerasian basin to 1 Wm^{-2} in deep Eurasian basin, and up to 5–10 Wm^{-2} Eurasian basin margins. Evidence of this has been observed as stepwise thermocline with sequences of well-mixed layers separated by thin interfaces where density

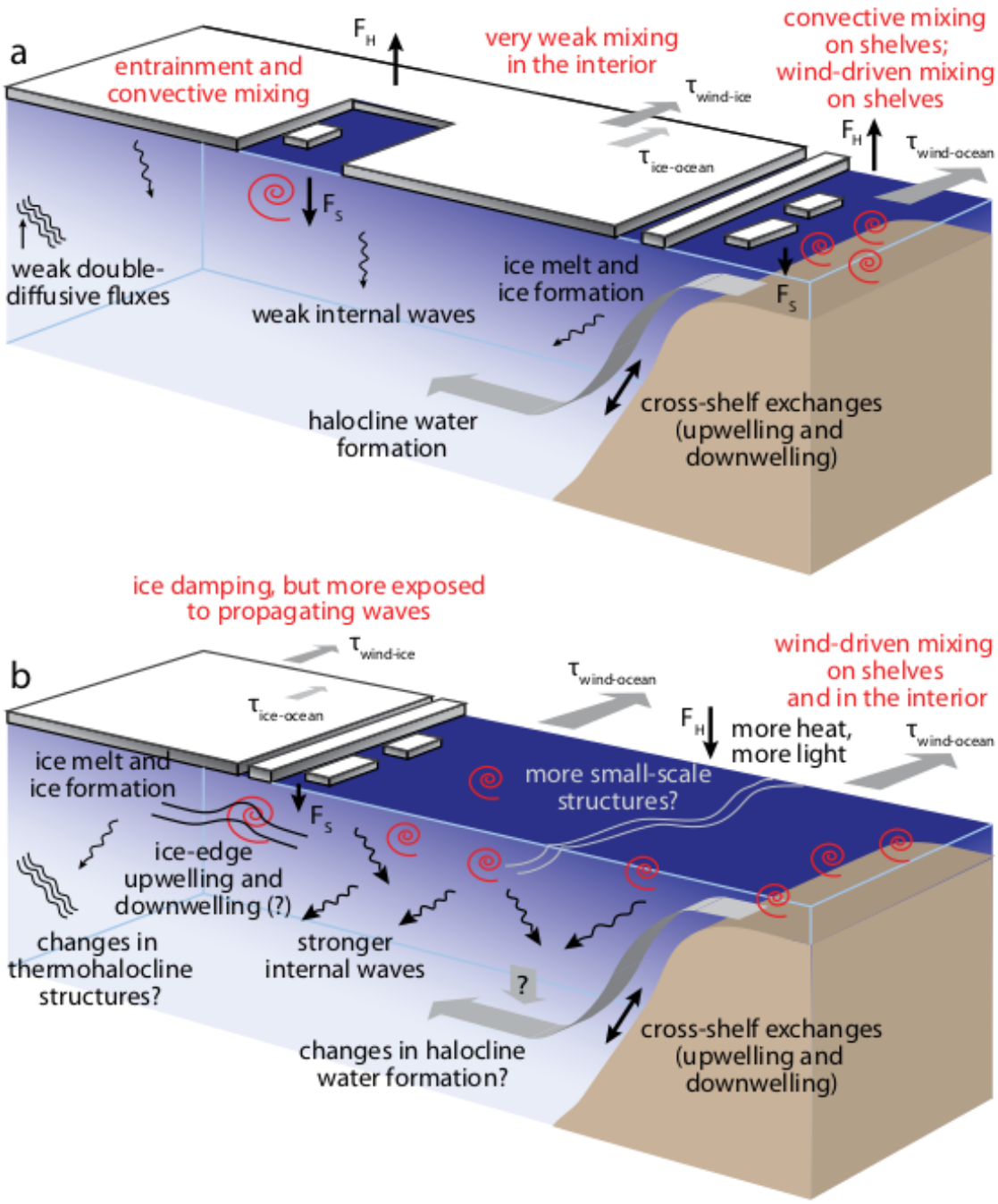

Figure 2.4: (a) The main mixing processes in ice covered Arctic. (b) The possible mixing processes under diminishing ice cover. Source: Rainville et al. (2011).

changes abruptly (Shibley et al., 2017). Although double-diffusion is near-insignificant to circulation, it can influence temperature and salinity on a regional scale away from the boundaries (Merryfield et al., 1999).

2.2.5 Parametrisation of convection

As mentioned the hydrostatic approximation leads to the elimination of vertical advection (convection) from the primitive equations. Therefore, how an ocean model handles instabilities in a water column that would without the hydrostatic approximation result in convection, is of crucial importance in the AO and also in global models to simulate deep-water formation (Griffies, 2004). The turbulent closure scheme (see section 2.2.3) resolves an unstable vertical profile by including the N^2 stability term in the calculation of diffusivities. Essentially, when the water column becomes unstable, $N^2 < 0$ and the vertical diffusivities increase.

Other methods include the convective adjustment and enhanced vertical diffusion. In convective adjustment, the vertical density profile is checked for instabilities ($N^2 < 0$) and if a part of the column is found unstable, its temperature and salinity are instantaneously mixed with the layer below and if as a result the layer below becomes unstable, the process is repeated until the water column is neutrally stable (Madec et al., 2017). Lastly, in enhanced vertical diffusion, in regions of unstable stratification ($N^2 < 0$), vertical eddy mixing coefficients are assigned to very large values to simulate convection (Madec et al., 2017).

Zhang and Steele (2007) examined the effect vertical mixing has on ocean stratification and distribution of salinity in the Canada Basin. They found that the strength of vertical mixing affects the modelled hydrography and circulation. If the vertical mixing, or convection, is too weak, the ocean model will simulate a stratification that is too strong and the Canada Basin circulation is anticyclonic in the upper layer and cyclonic below. This can cause the temperatures to be warmer while the surface layer is colder, thinner and fresher than observations. On the other hand, if the convection is too prominent, the stratification is too weak and dynamic, leading to anticyclonic circulation in the Canada Basin at all depths. Hence, the choice on the parametrisation is of crucial importance to representativeness of the model in the AO.

2.2.6 Ekman transport

In the AO, Ekman transport can occur due to stresses at three boundaries: atmosphere-ocean boundary layer, ice-ocean boundary layer and the bottom boundary. Local upwelling or downwelling can also occur at the ice-edge due to discontinuities in surface stresses (Yang, 2006). As mentioned, in ocean models the surface stresses take in account the fractions of ice and ocean (see Equation 2.3). The Ekman transport can be calculated:

$$-fv_{Ekman} = \frac{\tau^x}{\rho D_E} \tag{2.39}$$

$$fu_{Ekman} = \frac{\tau^y}{\rho D_E} \tag{2.40}$$

where D_E is the Ekman layer depth (approximately 18 m for the AO), u and v the vertically averaged Ekman velocities (Yang, 2006). Yang (2006) found that during their 26-year study period, Ekman transport varied the most in the Beaufort Sea and Fram Strait where there are large seasonal variations in ice motion and wind, while the maximum Ekman pumping rate was found to be 10 cm day^{-1} during winter. They also found that the heat advection was highest in the Beaufort and Chukchi Seas, and more pronounced during autumn.

The hydrography of deep waters in the AO is affected by bottom terrain, bottom shear and tides. Essentially, in the bottom boundary layer, friction is created due to bottom topography. In order to accurately solve circulation in the AO, realistic ocean bottom topography needs to be allowed by the model resolution which at this stage is too computationally demanding (Aksenov et al., 2010). Similarly as below ice or at the surface, in the ocean bottom, friction is often applied as a condition on vertical diffusive flux:

$$A^{vm}(\partial_z U_h) = F_h^U \tag{2.41}$$

where A^{vm} is the vertical diffusion coefficient and F_h^U is the downward flux of horizontal momentum inside the logarithmic turbulent boundary layer (Madec et al., 2017). F_h^U is often parametrisised in models as a linear or quadratic bottom friction (Madec et al., 2017). See Madec et al. (2017) for details.

2.2.7 Tides

Tides are one of the key processes altering the hydrography in the shallow shelf seas of the AO. Although tides affect processes in the surface by altering the sea ice dynamics and in ocean interior by affecting heat flux, they are rarely included in ocean models (Holloway and Proshutinsky, 2007). Tides induce sea ice movement which opens and closes areas of sea ice causing new ice formation, enhanced heat flux and ridging (Proshutinsky et al., 2005). These processes in turn lead to changes in albedo, brine fluxes and convection (Proshutinsky et al., 2005). The effects on sea ice, however, are compensated for by the net ice growth associated with polynyas (Holloway and Proshutinsky, 2007). Tidal mixing can be parametrisised using the vertical eddy diffusivity where additional diffusivity (K^{vT}) arises from internal tide breaking:

$$K^{vT} = q\Gamma \frac{E(x,y)F(z)}{\rho N^2} \tag{2.42}$$

where *E(x,y)* is the transfer of energy from barotropic tides to baroclinic tides, N is the Brunt-Väisälä buoyancy frequency, Γ is the mixing efficiency, q the tidal dissipation

efficiency and *F(z)* the vertical structure function (Madec et al., 2017). See Madec et al. (2017) for details.

3. Materials and methods

In this chapter, the materials and methods used in this study are presented and discussed.

3.1 Materials

3.1.1 ORAs

The analysis was performed on 11 Ocean Reanalysis products freely available at the Ocean Reanalyses Intercomparison Project database hosted by the Integrated Climate Data Center (ICDC) at Hamburg University. The data comes in NetCDF format and has been interpolated to the common regular $1^\circ \times 1^\circ$ latitude-longitude grid allowing for intercomparison. Uotila et al. (2018) chose ten ORAs, TOPAZ4. C-GLORS025v5, ECDA3, GECCO2, GLORYS2v4, GloSea5-GO5, MOVE-G2i, ORAP5, SODA3.3.1 and UR025.4, to be assessed due to their overlap over 1993-2010. As this study is a continuation on their ORA mean state study, the same ten ORAs and in addition ORAS5, an update of ORAP5, were chosen and collected from the database for the temporal analysis.

The key information (e.g. names and institutions, ocean model, forcing, main assimilation methods and assimilated data) of the ORAs used in this study are presented in Table 3.1. The differences between ORA outputs result from their different configurations. The uncertainties can originate from the model, forcing, assimilation method or even the assimilated data itself. In ocean model design, the errors can arise starting from the choice of the coordinate system, resolution or algorithms (Fox-Kemper et al., 2019). Detailed discussion on the effect of fundamental model design, including for example the choice of coordinates, has been presented by Griffies et al. (2000). Other sources of error are the initial conditions, parametrisations and boundary conditions, as they all play an important role in the formulation of the model (Fox-Kemper et al., 2019). The Arctic Ocean Model Intercomparison Project (AOMIP) has evaluated differences between models and observations, and between model outputs, arising, for example, from the different model configurations, forcing and parametrisations (Proshutinsky et al., 2001, 2011). They have identified common model shortcomings

Table 3.1: Descriptions of the Ocean Reanalysis Products used in this study

Product (Institute)	Ocean (resolution) - Ice model	Forcing	Main assim. method	Data assimilated	Data source	Relax to climate	Source
C-GLORS025v5 (CMCC)	NEMO3.2 (0.25, 50 z-levels)- LIM2	ERA-Interim	3DVAR	T, S, SSH, SST	EN3v2a, AVISO	Large scale bias corr. to EN3v2a	Storto et al. (2016)
ECDA3 (GFDL/NOAA)	MOM4 (1, 50 z-levels)- SIS	Coupled	EnKF	T, S, SST	HadSST, OISST, WOD09, GTSPP, Argo	fully coupled	Chang et al. (2013)
GECCO2 (Hamburg University)	MITgcm (1 x 1/3, 50 z-levels)	NCEP RA1	4DVAR (adjoint)	T, S, SSH, SST	EN3v2a, AVISO, GOCO, HadISST, AMSRE, WOA09	None	Köhl (2015)
GLORYS2v4 (Mercator Océan)	NEMO3.1 (0.25, 75 z-levels)- LIM2	ERA-Interim	reduced order order KF + 3DVAR large scale bias corr. to in-situ T & S	T, S, SSH, SST	CMEMS, NOAA AVHRR	T, S restoring towards EN4.1.1 for z >2000 m & lat < 60 °S ($\tau = 20$y)	Garric et al. (2018)
GloSea5-GO5 (UK MetOffice)	NEMO3.4 (0.25, 75 z-levels) - CICE	JRA-55	3DVAR	SST, SSH SST, SSH	EN4, ICOADS, AVHRR, ATSR, AMSRE, AVISOv3	Surface Haney restoring + 3D t/s ($\tau = 1$y)	Blockley et al. (2014b) Blockley et al. (2014a)
MOVE-G2i (MRI/JMA)	MRI.COM3 (1 x 0.3-0.5, 52 z-levels) - CICE4	JRA-55	3DVAR	T, S, SSH, SST	WOD13, GTSPP, AVISO, MGDSST	Relaxing T/S to merged PHC3-WOA13 climatology ($\tau = 5$y)	Toyoda et al. (2016)
ORAP5 (ECMWF)	NEMO3.4 (0.25, 75 z-levels)- LIM2	ERA-Interim	3DVAR	T, S, SSH, SST	EN3v2a, AVISO, OSTIA	Relaxation to OSTIA/ NOAA OIv2d SST	Zuo et al. (2015) Tietsche et al. (2015)
ORAS5 (ECMWF)	NEMO3.4 (0.25, 75 z-levels) - LIM2	ERA-Interim	3DVAR		HadISST2 SST, OSTIA SIC, EN4 in-situ, AVISO DT2014 SLA		Zuo et al. (2019)
SODA3.3.1 (University of Maryland)	MOM5 (0.25, 50 z-levels)- SIS	NASA MERRA2	OI	T, S, , SST	WOD, ICOADS, AVHRR, Metosat SEVIRI	Restoring to mean T & S ($\tau = 10$y). Relaxation to WOA SSS ($\tau = 3$m)	Carton and Giese (2010)
TOPAZ4 (NERSC)	HYCOM (12-16 km, 28 z-levels) - EVP SI	ERA-Interim	EnKF	T, S, SSH, SST	NOAA Reynolds, OSTIA, CLS, Damocles	Relaxing T/S to merged PHC3-WOA13 climatology	Xie et al. (2017) Sakov et al. (2012)
UR025.4 (University of Reading)	NEMO3.2 (0.25, 75 z-levels) - LIM2	ERA-Interim	OI	T, S, SSH, SST SSS	EN3v2a	None	Valdivieso et al. (2014)

in the AO, such as, disparities in the transports across the Fram Strait, lack of a cold halocline in the Amerasian Basin and misrepresentation of the AW temperature, all important features affecting the hydrography of the AO (Steiner et al., 2004). As discussed in the previous chapter, these shortcomings result from the finite-grid size limiting the ability of the models to resolve eddies and related dynamics, and the exclusion of processes such as shelf water formation and tides in model physics (Steiner et al., 2004).

All of the ORAS, except for GECCO2, are hydrostatic and therefore some important physical processes affecting the hydrography of the AO, such as convection, are parametrised. GECCO2, however, utilises MIT general circulation model (Adcroft et al., 2019) that uses the full incompressible, nonhydrostatic Navier-Stokes equations including the tendency, advective and diffusive terms (Kantha and Clayson, 2000) For the AO, GECCO2 has 40 km resolution and uses the dynamic-thermodynamic sea ice model by Zhang and Rothrock (2000). As discussed in the previous chapter, the grid size can limit the ability of the ORAs to fully resolve eddies in the AO. Ten of the eleven ORAs are of global extent, while TOPAZ4, a coupled ocean-sea ice data assimilation (DA) system, is a regional Arctic-North Atlantic product using the model HYCOM with a grid size of 12-16 km. HYCOM is an oceanic general circulation model framed in hybrid isopycnic-Cartesian coordinates (Hunke and Dukowicz, 1997). TOPAZ4 uses the sophisticated assimilation method, ensemble Kalman Filter. Even though TOPAZ4 uses isopycnic coordinates, Xie et al. (2017) found that TOPAZ4 is more successful in modeling near-surface ocean than subsurface ocean due to models limitations to maintain AW and degradation of the assimilation when the measurements are sparse.

ECDA3 (Ensemble Coupled Data Assimilation) has the coarsest grid-size out of the 11 ORAs, the common 1 ° x 1 ° grid. ECDA3 was purposely left out from the ensemble mean in this study due its coverage being more restricted in the AO than the other ORAs. However, ECDA3 is the only fully coupled climate-ocean model while the other ORAs need surface forcing to account for the atmosphere-ocean exchange. Most of the ORAs are forced by European Centre for Medium-Range Weather Forecasts (ECMWF) global atmospheric reanalysis ERA-Interim. The two ECMWF's ORAs, ORAS5 and ORAP5 use the same ocean model, NEMO v3.4.1 (see Madec et al., 2017). The use of a tripolar grid allows for eddies to be presented north of 50 °N and the model resolution is 9 km at best in the AO (Zuo et al., 2019). The model is coupled with a sea ice model, Louvain-la-Neuve (LIM2) (see Fichefet and Maqueda, 1997). Coupling the ocean model with a sea ice model is important as most of the AO thermodynamics and physics are closely related to sea ice dynamics. An earlier version of NEMO coupled with the LIM2 sea ice model is also utilised by C-GLORS025v5 (NEMO3.2), GLORYS2v4 (NEMO3.1) and UR025.4 (NEMO3.2). LIM2 is a dynamic-thermodynamic model that uses viscous-plastic rheology with three layer scheme similar to Semtner (1976) with one snow and at least 2

ice layers. Other sea ice models used by the ORAs are Sea Ice Simulator (SIS), which is a dynamic-thermodynamic model that uses elastic-viscous-plastic rheology and the Los Alamos sea ice model CICE (Hunke and Dukowicz, 1997; Hunke et al., 2015).

Most of the ORAs are relaxed to climatology to prevent the model from drifting. This means their 3-dimensional T/S or Sea Surface Salinity (SSS) are checked against known climatology and corrected accordingly (Shi et al., 2017). The relaxation time intervals differ between ORAs, range from 1 year (GloSea5-GO5) to 20 years (GLORYS2v4). Unlike other ORAs, GECCO2 and UR025.4, are not relaxed to climatology.

To better the model-only results, observations are assimilated in to the product. In the data assimilation (DA) process, the first guess of a model is corrected based on observations and an error-estimation, to produce an evolving state of the ocean, the analysis (ECMWF, 2019; Warner, 2011). A weighing factor is applied to the difference between model's first guess and observations in order to determine the amount of correction required to produce the analysis (Warner, 2011). The ORAs chosen for this study all use least squares assimilation methods, including optimal interpolation (OI), variational method (3DVAR), 4D variational method (4DVAR) and Kalman Filter. Least squares methods aim to produce the best result by minimising the cost function to ensure the analysis does not drift too far from observations and model outputs. Least squares minimisation (Kalman Filter):

$$\mathbf{X_i^a} = \mathbf{X_i^f} + \mathbf{K_i}(\mathbf{Y_i} - \mathbf{HX_i^f}), \tag{3.1}$$

where $\mathbf{X_i}$ is the ensemble of model state vectors, $\mathbf{Y_i}$ is the matrix of perturbed observations and $\mathbf{H}$ the observation operator (Xie et al., 2017). The subscripts a and i stand for analysed and forecasted states (Xie et al., 2017). $\mathbf{Y_i} - \mathbf{HX_i^f}$ is the departure from model to observations (Xie et al., 2017). $\mathbf{K_i}$ is the Kalman gain (see Evensen, 2003).

The least squares methods mainly vary on how they handle the forecast error covariances. Ensemble Kalman Filter (EnKF) is often seen as the most sophisticated out of the aforementioned DA methods as it allows for time evolving error covariances while OI and 3DVAR methods assume the covariances to be largely homogeneous in time (Houtekamer and Mitchell, 1997). The EnKF is computationally demanding and hence mainly used in regional studies, such as for the AO (TOPEZ4). 4DVAR, although less sophisticated, is less expensive method that also allows time evolvement in the error covariances as it includes time dimension to the analysis (Houtekamer and Mitchell, 1997).

3.1.2 EN4.2.0.g10

The ORAs were compared to observations based product EN4.2.0.g10 (Good et al., 2013). EN4.2.0.g10 data set consists of quality-controlled profiles of ocean temperature and salinity from across the ocean from 1900 to present (Good et al., 2013). The main data source

for EN4 is the World Ocean Database (WOD09). The coverage of WOD09 is limited in the Arctic, and hence other sources are included to increase the spatial coverage, including Argo, Arctic Synoptic Basin Wide Oceanography (ABSO) and Global Temperature and Salinity Profile Program (GTSPP) (Good et al., 2013). ABSO is a compilation of multiple sources itself: Hydrobase, the Physical and Chemical Properties from Selected Expeditions in the Arctic Ocean project, the Beaufort Gyre Experiment, the North Pole Environmental Observatory (NPEO), the Freshwater Switchyard of the Arctic project, and the Nansen and Amundsen Basins Observational System (NABOS) and the Canadian Basin Observational System (CABOS) (Good et al., 2013).

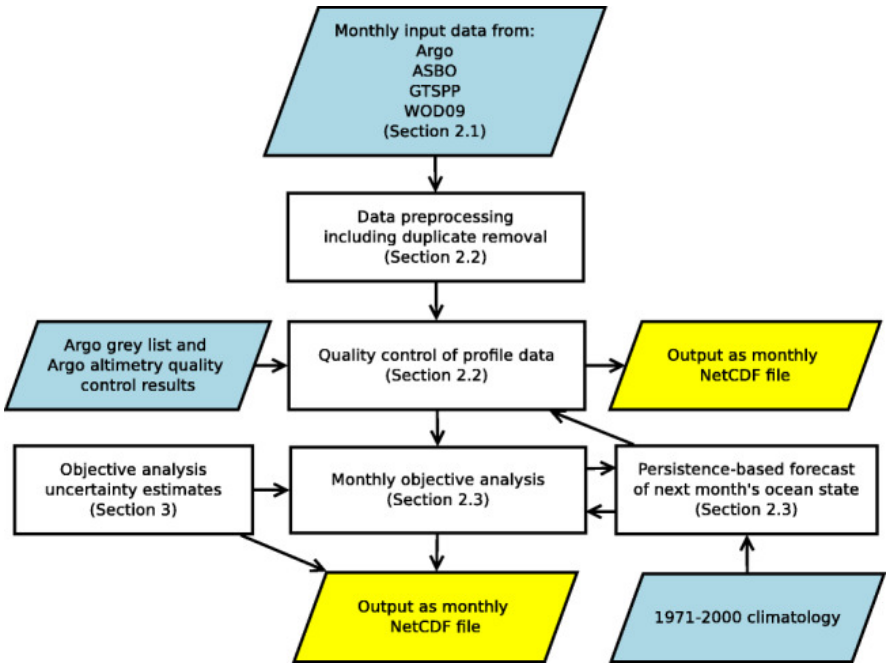

Figure 3.1: Structure of the EN4. Source: Good et al. (2013).

The journey from data sources to finished product can be seen in Figure 3.1. Quality control is performed on the input data and Argo-profile duplicates are removed from WOD09 and GTSPP data sets (Good et al., 2013). The quality controlled data is then used in monthly potential temperature and salinity objective analyses (Good et al., 2013). These analyses combine a background ocean state from the previous month's objective analysis with the quality controlled data from the month being analysed, using an iterative method in solving the optimal interpolation (OI) equations (Good et al., 2013). Information on the covariances in the possible errors in the observations and the background are needed to carry the analyses and the errors are assumed to be uncorrelated (Good et al., 2013). If there's no observations present, the analyses relax to the climatology (Good et al., 2013).

3.2 Methods

The focus of this study is on the hydrography of the AO. Hydrography is a field that aims to describe the physical, quantifiable features of a water body, such as tides, currents, temperature and salinity. Only potential temperature and salinity were considered in the scope of this study. The analysis was carried out with Python 3.6.

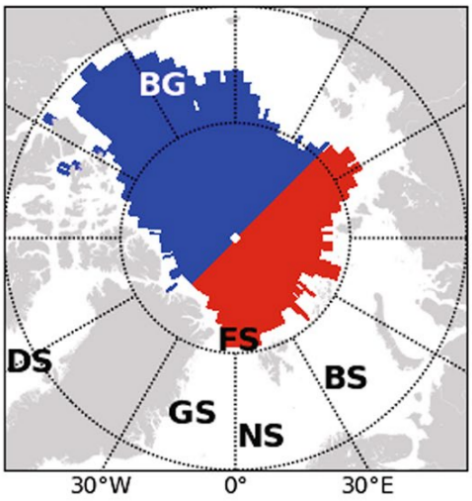

Figure 3.2: Grids, where depth >500 m, belonging to the Eurasian Basin in red and the Amerasian Basin in blue. Annotations: the Fram Strait (FS), Beaufort Gyre (BG), Barents Sea (BS), Davis Strait (DS), Greenland Sea (GS) and Norwegian Sea (NS). Source: Uotila et al. (2018).

Depth and area masks were applied on the data to eliminate shallow near-coastal regions from the analysis as they could introduce error to the analysis. World Ocean Atlas 2013 Land-Sea $1° \times 1°$ mask was used to eliminate areas where the water depth was less than 500 m (see Figure 3.2). The area mask was applied to allow for separate trend analysis of Amerasian and Eurasian basins (Figure 3.2). Accordingly, the AO was split into two basins along two meridians 135°E 45°w following the Lomonosov Ridge. Both basins were further divided into five depth layers, 0–100 m, 100–300 m, 300–700 m, 700–1500 m and 1500–3000 m.

The data was provided as Ocean Heat Content (OHC) and Ocean Salinity Content (OSC), which are vertically integrated potential temperature and salinity, respectively. From these the mean potential temperature and salinity were calculated for each layer:

$$\langle X_{L \to U} \rangle = \frac{OXC_{L \to 0} - OXC_{U \to 0}}{L - U} \tag{3.2}$$

where X is either temperature or salinity, OXC is either OHC or OSC and $\langle X_{L \to U} \rangle$ is the average between depths L and U (Uotila et al., 2018).

The ensemble approach has been highlighted in ORA inter-comparison studies (Shi et al., 2017; Uotila et al., 2018). The multi-model mean is considered to be at least

as accurate representation of reality than the best performing ORA and sometimes even better than any single ORA (Masina et al., 2017). Accordingly, the MMM was also formed for this study from 10 of the studied ORAs:

$$\overline{X_{MMM}} = \frac{1}{nsys} \sum_{n=1}^{nsys} X_n \tag{3.3}$$

where *nsys* is the number of ORAs (Shi et al., 2017). The MMM is a desirable method as it dampens out any deviating behaviour of an ORA but it is possible for all the ORAs to suffer from similar configurational biases not caught by the MMM (Shi et al., 2017).

The OHC and OSC data were used to formulate yearly time series of potential temperature and salinity. The time-average for the individual ORAs ($\overline{X_{i,j}}$), MMM and EN4.2.0.g10 were calculated over the time period (1993–2010) and using the time-average, anomalies (X_A) were calculated:

$$X_A(i,j,t) = X_n(i,j,t) - \overline{X_n(i,j)} \tag{3.4}$$

These anomalies were averaged spatially for each basin and the Fram Strait, and plotted into time series for each integrated depth layer. Some of the data had a time resolution of a day, some of a month and some of a year, hence the data were first yearly averaged before any trends were calculated. The basin-wide potential temperature and salinity trends were calculated for each depth layer for the Amerasian and Eurasian Basins. To get more detailed information, trends over the study period were calculated for each layer and also plotted per-grid to allow for temporal analysis with only trends significant at 0.05 level being displayed.

Similar analysis has not been carried out before for the AO and the paucity of observations complicates the assessment of the reality. Although the ORAs are compared to EN4.2.0.g10, the observational product can also suffer from errors and biases resulting from statistical methods and data gaps. Hence, to get a sense of the error involved in the spatial spread of the trends, per-grid standard deviation was calculated for each basin, product and depth layer as follows:

$$STD_X(i,j,t) = \sqrt{\frac{1}{yrs} \sum_{t=1}^{yrs} (X(i,j,t))^2} \tag{3.5}$$

where *yrs* is the number of years (17), i and j are the longitude and latitude and X is the annual mean of individual ORA (Shi et al., 2017). Standard deviation in its essence is a statistical method to measure the dispersion of time series relative to its mean. The STD was also calculated for the ORA MMM. Shi et al. (2017) also used the ensemble spread (SPD) in order to measure the 'noise', or uncertainty of the MMM (or EMORA in their paper):

$$SPD_{MMM}(i,j) = \sqrt{\frac{1}{nsys} \sum_{n=1}^{nsys} (X_n(i,j) - \overline{X_{MMM}}(i,j))^2} \tag{3.6}$$

where *nsys* is the number of ORAs. As discussed when presenting the materials of this study, the ORAs can contain systematic errors caused by their configuration. The SPD is a good indication on the spread of the error but as Shi et al. (2017) noted, all of the ORAs can contain same systematic errors not flagged by the SPD. Hence the errors presented by STD and SPD cannot be considered as a 'true error' (Shi et al., 2017).

4. Results

This chapter presents the results of the study. First the anomaly time series for OHC and OSC in 0–700 m are presented for the Eurasian and Amerasian Basins and for the Fram Strait. Then, the overall basin-wide trends in temperature and salinity for both basins and for the three depth layers, 0–100 m, 100–300 m and 300–700 m, are displayed. Results for the deeper layers are not shown here. Lastly, the per grid trends in temperature and salinity are presented for the three layers, including the per grid ORA STD and ORA SPD analyses.

4.1 The Eurasian Basin

4.1.1 OHC anomalies

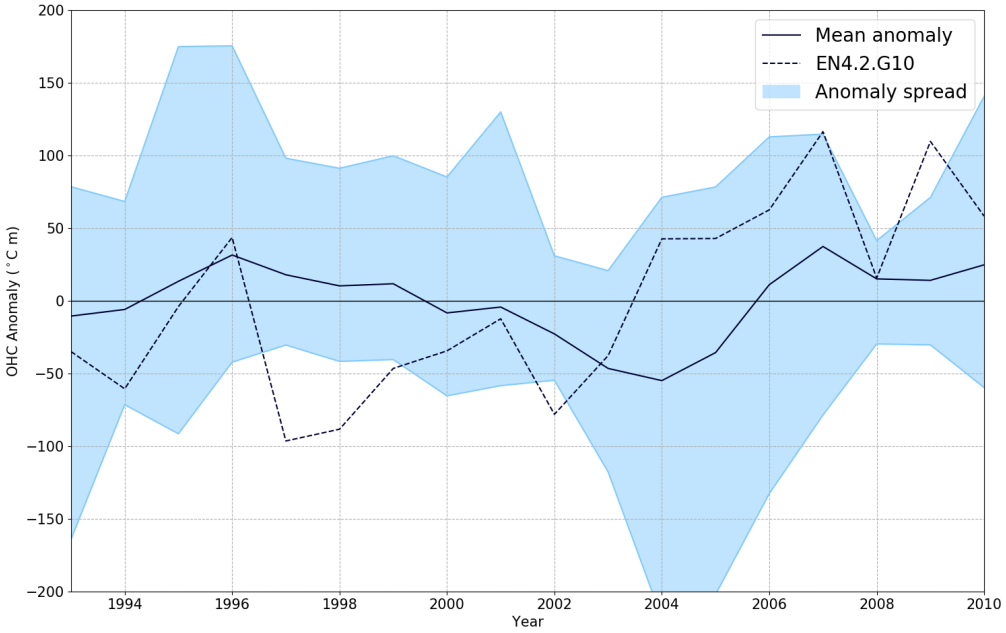

Figure 4.1: 0-700 m OHC anomalies for the Eurasian Basin for the ORA mean anomaly and EN4.2.0.g10 (dashed) for years 1993–2010. The ORA spread (minimum and maximum anomaly) is visible as blue shadow.

Yearly ocean heat content (OHC; °Cm) anomalies for 0–700 m layer over the study period for the Eurasian Basin can be seen in Figure 4.1. The anomalies appear variable from one year to another both in the MMM and EN4.2.0.g10. In the MMM the variability can be seen as colder anomalies being observed in 1993–1994, warmer anomalies 1995–1999, colder anomalies again 2000–2005 and warm anomalies again in 2006–2010. In EN4.2.0.g10 however, there are colder anomalies from 1993 to 2003 (with the exception of year 1996) and warmer anomalies there onward, reflecting a warming trend over the time period. It appears the observational product is more similar to the ORA spread minimum in the first half of the time period and maximum spread on the later half, than the ORA mean. The spread among the ORAs is remarkable, the MMM appears to dampen the drastic dips and peaks in the anomaly time series that can also be seen in the observation-only product. Both ORA mean and EN4.2.0.g10 agree on the anomalously warm year in 2007. Based on both the observational product and MMM, there is a clear warming trend over the Eurasian Basin over the later half of the study period.

4.1.2 OSC

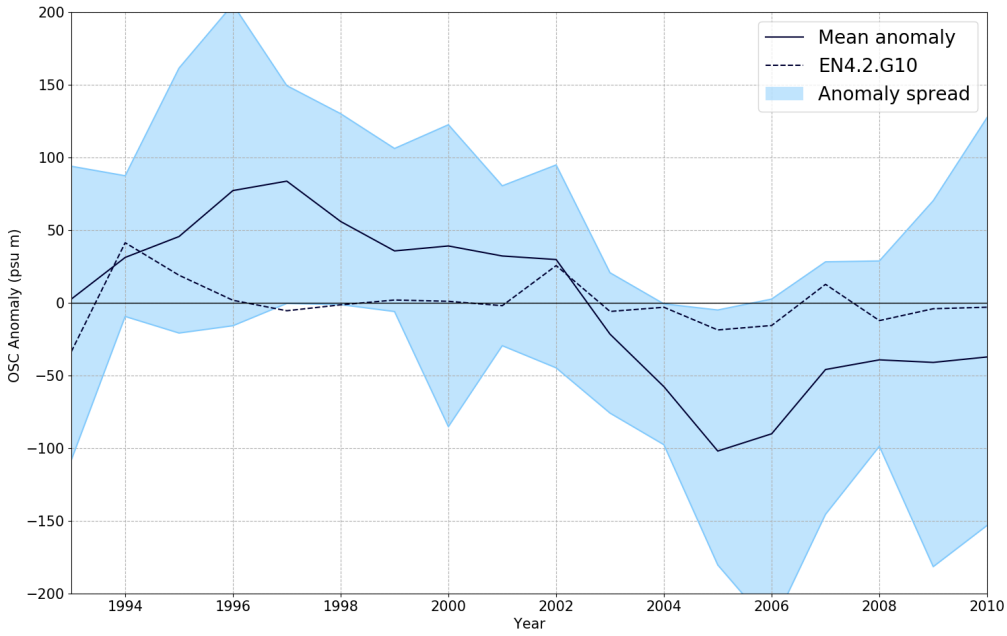

Figure 4.2: 0–700 m OSC anomalies for the Eurasian Basin for EN4.2.0.g10 and MMM for years 1993–2010. The ORA spread (minimum and maximum anomaly) is visible as blue shadow.

Yearly ocean salt content (OSC; PSU m) anomalies for 0–700 m layer over the study period can be seen in Figure 4.2. The ORA mean anomaly appears to be more saline than the time period average for the first half of the time series (1993–2002) and fresher

thereafter. The observational product, EN4.2.0.g10, has only subtle change over the time period from more saline to slightly fresher anomalies. The shift in both seems to occur between 2002 and 2003. Based on both the observational product and MMM, there is a clear freshening trend over the Eurasian Basin over the study period, perhaps over-estimated by the MMM or under-estimated by the EN4.2.0.g10. It is worth noting that most ORAs, with the exception of GECCO2 and TOPAZ4, show more saline anomalies over 1993–2003 and more fresh anomalies there after. There appears to be a fresh anomaly peak in 2005–2006 where also the maximum anomaly ORA spread appears to be fresher than the mean over the time series.

4.2 The Amerasian Basin

4.2.1 OHC

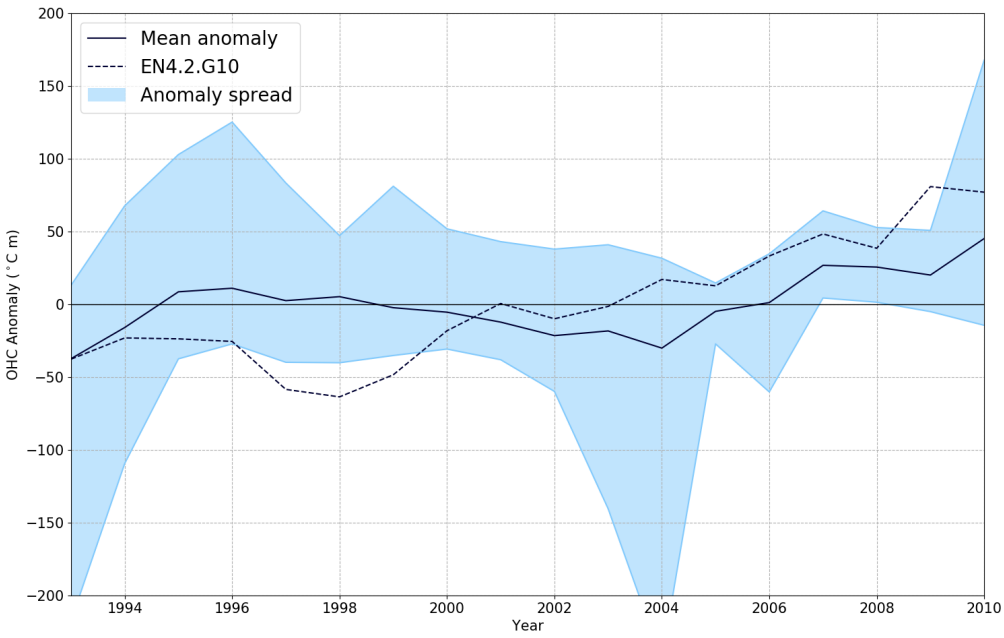

Figure 4.3: 0–700 m OHC anomalies for the Amerasian basin for EN4.2.0.g10 and MMM for years 1993–2010. The ORA spread (minimum and maximum anomaly) is visible as blue shadow.

Yearly ocean heat content (OHC; °Cm) anomalies for 0–700 m layer over the study period for Amerasian Basin can be seen in Figure 4.3. The observational product, EN4.2.0.g10, shows a clear trend from colder-than-average OHC from 1993–2003 to warmer-than-average 2004–2010. The ORAs, however, show clear decadal variability compared to EN4.2.0.g10. Where EN4.2.0.g10 starts to show warmer anomalies in 2004, the MMM appears to be biased by the minimum anomaly (less than -200 C°m) of the ORA anomaly

spread. The anomaly spread, however, decreases towards the end of the study period, showing clear warming from 2004 to 2010.

4.2.2 OSC

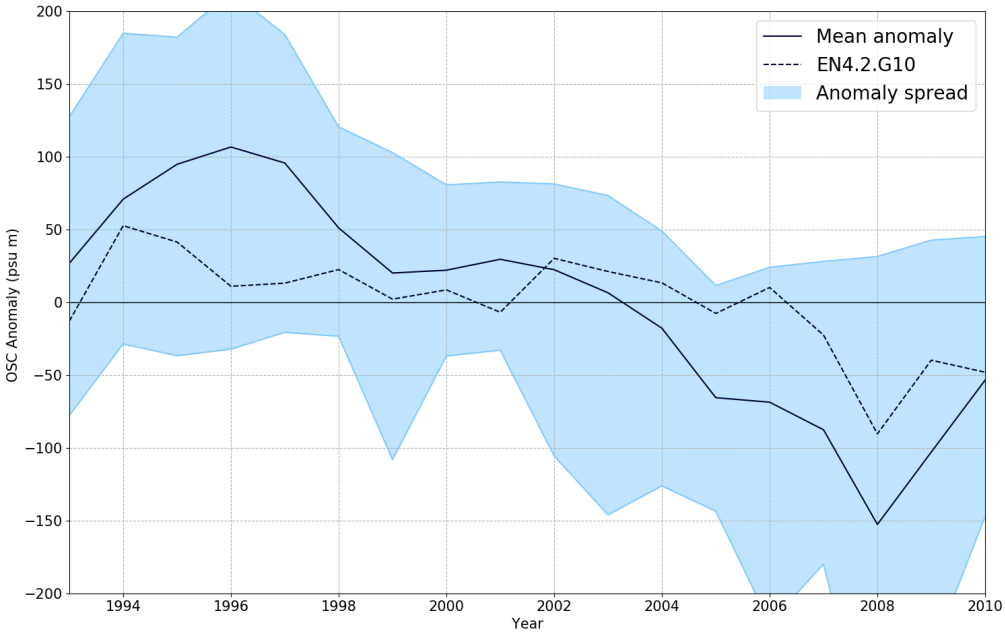

Figure 4.4: OSC anomalies for the Amerasian basin for EN4.2.0.g10 and MMM for years 1993–2010. The ORA spread (minimum and maximum anomaly) is visible as blue shadow.

Yearly ocean salt content (OSC; PSU m) anomalies for 0–700 m layer over the study period can be seen in Figure 4.4. For the Amerasian Basin, the OSC anomalies appear to be of a greater magnitude for the MMM than for the EN4.2.0.g10. Similarly to the Eurasian Basin, both show more saline anomalies over the beginning of the study period. The freshening seems to start in 2003 for MMM and in 2006 for EN4. Both the MMM and EN4.2.0.g10 show a year of fresher anomaly in 2008, two years after a similar dip in the Eurasian Basin OSC. The spread in ORA anomalies is great, from 150 to 300 PSU m. Regardless, the trend displayed by the ORA MMM is a clear freshening trend.

4.3 The Fram Strait

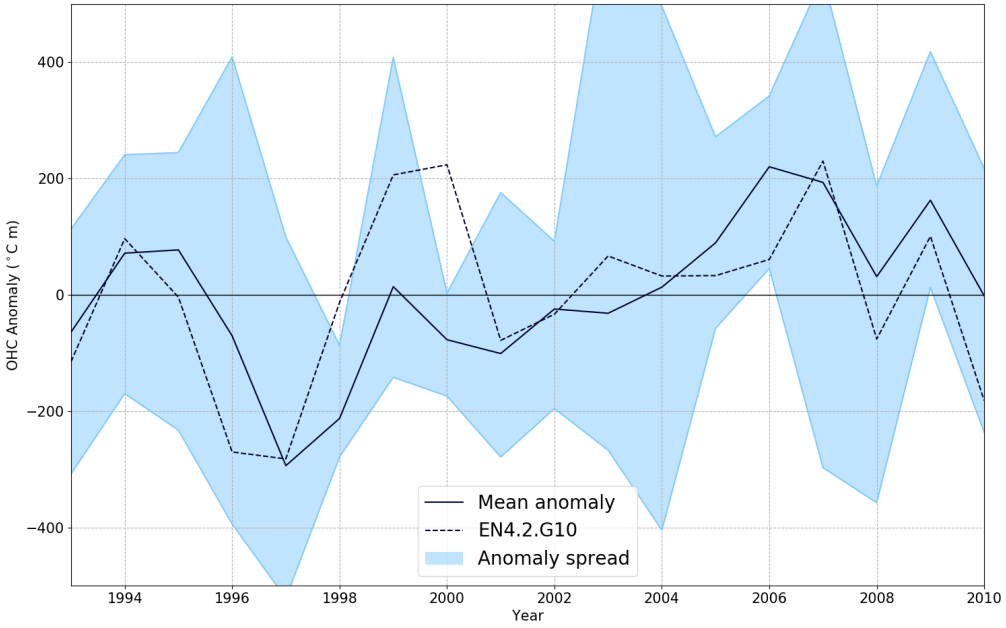

Figure 4.5: OHC anomalies for the Fram Strait for EN4.2.g10 and MMM for years 1993–2010. The ORA spread (minimum and maximum anomaly) is visible as blue shadow.

Yearly ocean heat content (OHC; °Cm) anomalies over the study period can be seen in Figure 4.5. For the Fram Strait the OHC anomalies are much greater in their spread than for the Eurasian and Amerasian Basins (note the y-axis scale is double that of Figure 4.1). Futhermore, the overall variability from one year to another is much greater, with warmer anomalies more prominent in the latter part of the study period. Although the spread amongst the ORAs is great, the MMM and the EN4.2.0.g10 show very good agreement in terms of the variability being similar from one year to another, showing warmer than average OHC from 2003 to 2009.

4.4 Basinwide trends in temperature and salinity

4.4.1 The Eurasian Basin

The overall trends in temperature (Figure 4.6) and in salinity (Figure 4.7) were calculated for the Eurasian Basin. In the 0–100 m layer, most of the ORAs seem to agree over a moderate warming trend of 0.03 °C/decade and freshening trend of -0.02 PSU/decade but no significant trend is visible in the observational product EN4.2.0.g10 for either. For the 100–300 m layer, EN4.2.0.g10 shows a strong warming signal of 0.25 °C/decade while

the ORAs are in disagreement with significant and insignificant signalling both warming and cooling in the layer. In terms of salinity, neither EN4.2.0.g10 nor MMM show a significant trend. For the 300–700 m layer, EN4.2.0.g10 shows a warming of 0.1 °C/decade and freshening of ∼ -0.001 PSU/decade while the ORAs are again in disagreement. No trends in temperature can be deduced from the 700–1500 m and 1500–3000 m layers with TOPAZ4 being an outlier with very strong warming trends. MMM, however, shows a slight trend in terms of freshening in the two deep layers.

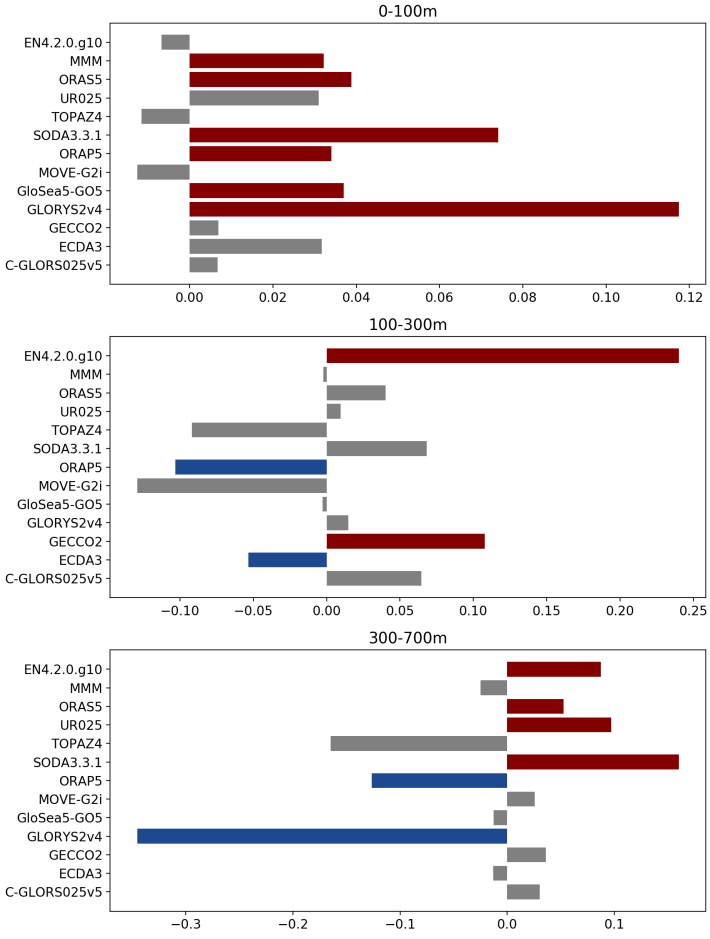

Figure 4.6: Temperature trends °C/decade for the Eurasian Basin. Significant trends are in color, increasing in red and decreasing in blue.

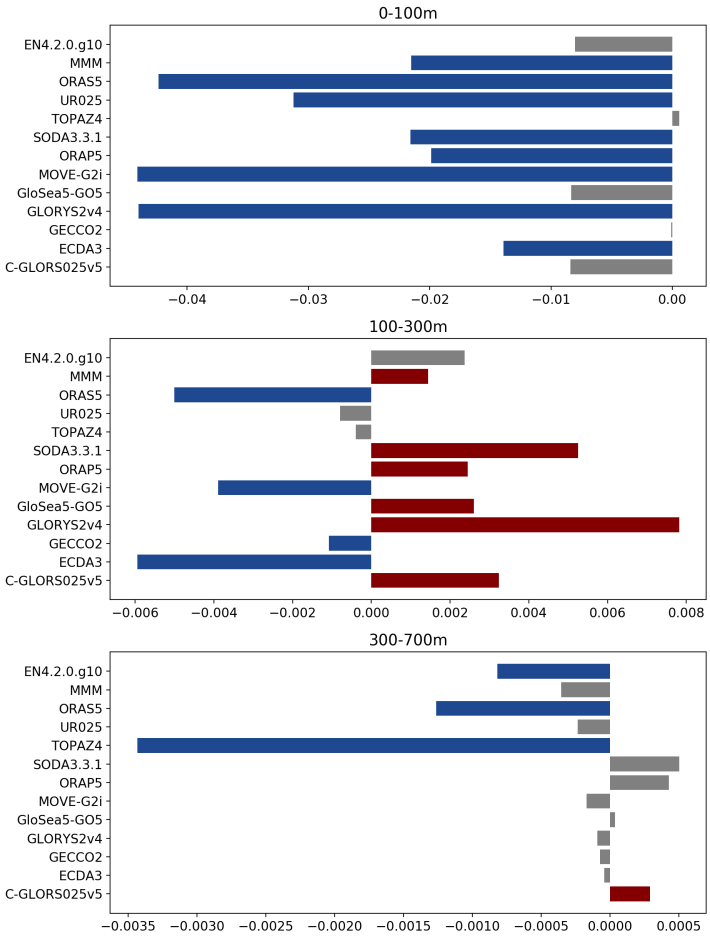

Figure 4.7: Salinity trends PSU/decade for the Eurasian Basin. Significant trends are in color, increasing in red and decreasing in blue.

4.4.2 The Amerasian Basin

The overall trends in temperature (Figure 4.8) and in salinity (Figure 4.9) were calculated for the Amerasian Basin. In the 0–100 m layer, neither the EN4.2.0.g10 nor MMM show a significant trend in temperature but most of the ORAs, excluding TOPAZ4 and SODA3.3.1, show a moderate increasing trend. In terms of salinity, both EN4.2.0.g10 and MMM show a strong freshening trend of -0.03 PSU/decade with the only outlier being GECCO2. For the 100–300 m layer, the MMM shows a warming trend of 0.03 °C/decade and a freshening trend of -0.005 PSU/decade while EN4.2.0.g10 shows a stronger warming signal of 0.1 °C/decade but has no significant trend in salinity. For the 300–700 m layer, both EN4.2.0.g10 and MMM show a warming signals of similar magnitude as for the 100–300 m layer but no significant trend is visible in terms of salinity. In the two deepest layers, 700–1500 m and 1500–3000 m, both EN4.2.0.g10 and MMM show a warming signal of ∼0.03 °C/decade while MMM also shows an increasing trend in salinity not visible in the observational product.

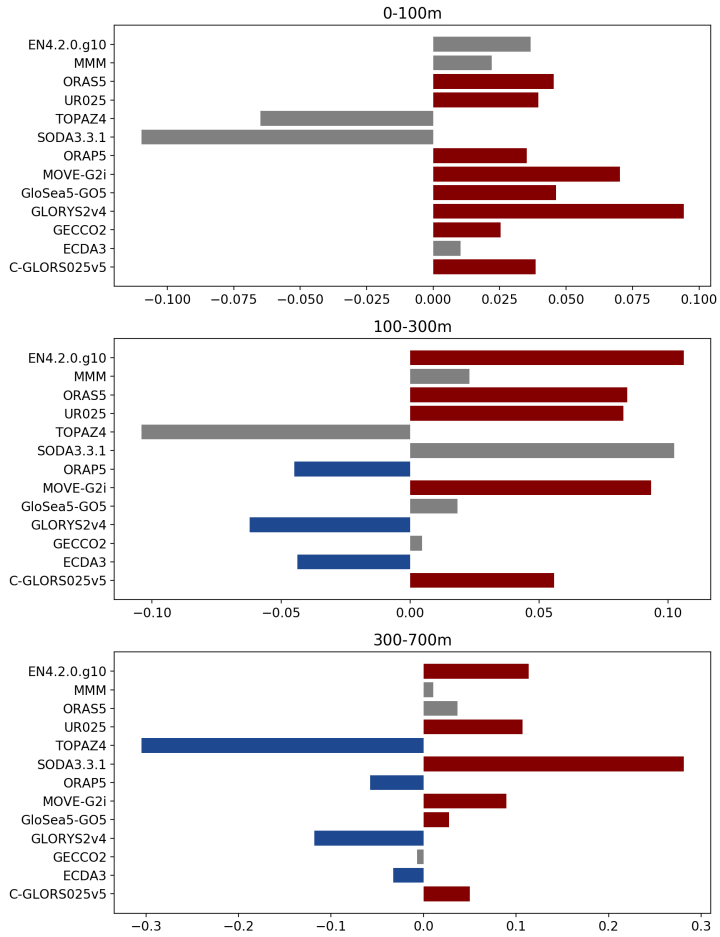

Figure 4.8: Temperature trends °C/decade for the Amerasian Basin. Significant trends are in color, increasing in red and decreasing in blue.

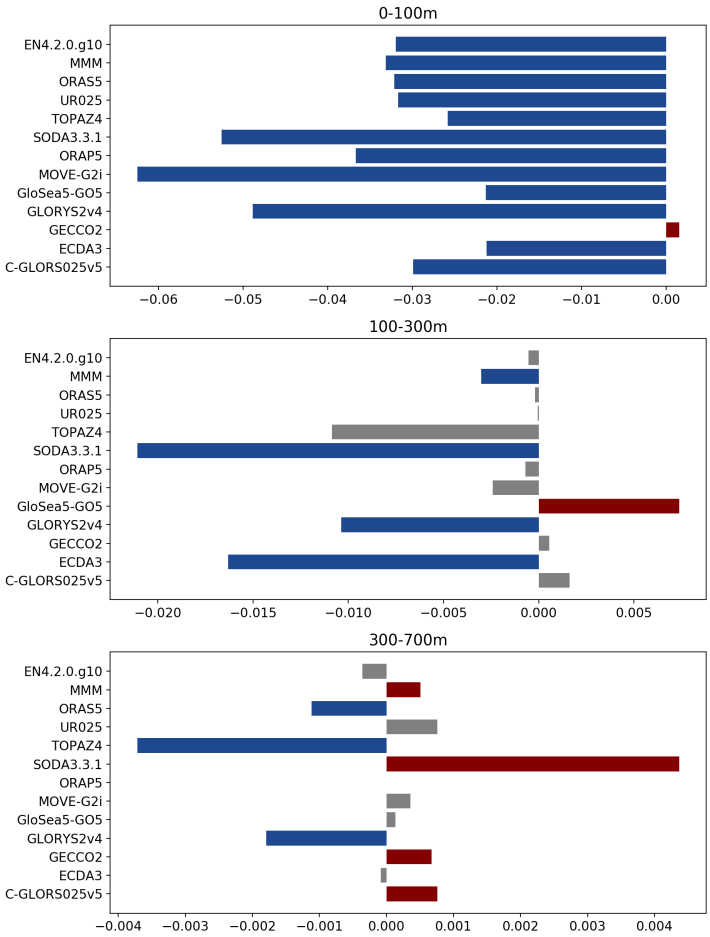

Figure 4.9: Salinity trends PSU/decade for the Amerasian Basin. Significant trends are in color, increasing in red and decreasing in blue.

4.5 Per grid trends in temperature and salinity

In this section, the observed, statistically significant trends in temperature and salinity are presented for each layer, starting with the uppermost 100 m (Figures 4.10; 4.11). For the central AO, more towards the Siberian Shelf Seas, the MMM shows a warming trend of 0.1 °C per decade. The trend doubles at the Nansen Basin, 0.2 °C per decade. The ORA SPD is from 0 up to 0.1 °C per decade for the area, meaning that the ORAs are in fairly good agreement with each other on the trend. The observational product, EN4.2.0.g10, does not show any significant trend for the central AO but a strong warming signal of up to 0.5 °C per decade in the Nansen Basin towards the Kara and Barents Seas. Similarly for the Beaufort Sea, EN4.2.0.g10 shows a strong warming trend of the same magnitude. The ORA SPD shows disagreement and noise of up to 0.5 °C per decade in the Beaufort Sea which is most likely the reason there is no significant trend in the ORA MMM. From the ORA STD, however, a strong signal of variability in the Beaufort Sea can

be seen. When looking at the individual ORAs (see Appendix A, Figure A.1), it appears that most of the ORAs are in agreement with the warming trend except for SODA3.3.1 and TOPAZ4. The ORA MMM and EN4.2.0.g10 show slightly differing trend north of Canadian Arctic Archipelago. The MMM shows a mild, localised warming trend while the EN4.2.0.g10 shows a mild cooling trend. East of Greenland, at/near Fram Strait, both the MMM and EN4.2.g10 show cooling with MMM trend being of magnitude -0.2 °C per decade while the EN4.2.0.g10 is at double of that. The MMM trend could be dampened by the strong disagreement between ORAs displayed in the ORA SPD for the Fram Strait.

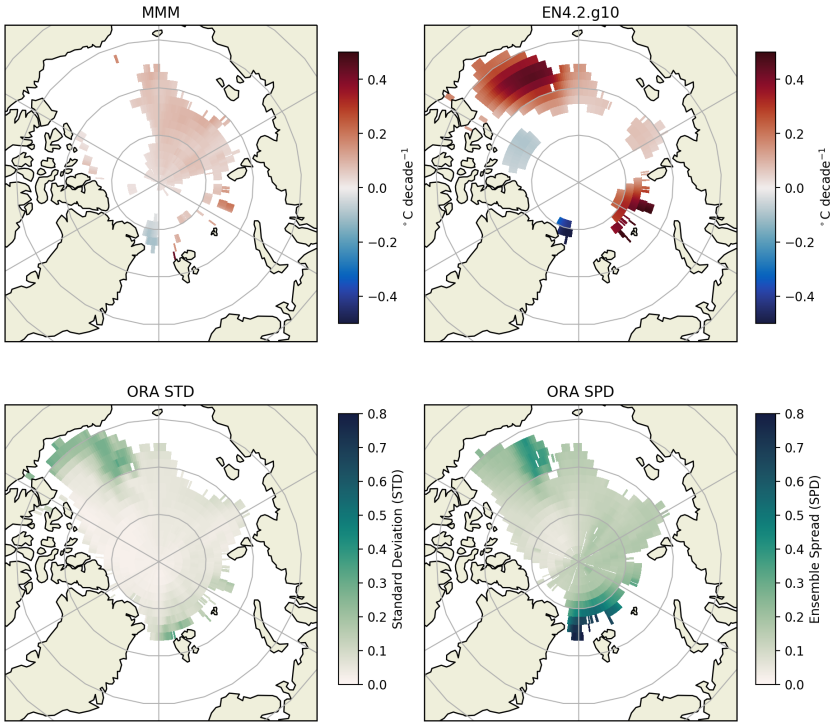

Figure 4.10: Temperature trends for the MMM and EN4.2.0.g10 and statistical analyses, ORA STD and ORA SPD, for the 0–100 m layer.

Trends in salinity are more straightforward to interpret (Figure 4.11). The MMM shows a clear freshening trend for the Amerasian Basin, from -0.25 PSU per decade in the central Amerasian Basin to -0.5 PSU per decade north of the Laptev Sea and at the Beaufort Sea. These observations are confirmed by the ORA STD. ORA SPD, however, shows very strong disagreement between the ORAs, especially for the Beaufort Sea. When looking at all of the individual ORAs (see Appendix A, Figure A.2), it appears that most are in agreement with the freshening trend (except for ECDA3 and GECCO2) but disagree on the location of the maximum trend. The EN4.2.0.g10 shows similar, but stronger, trend to the MMM of down to -0.8 PSU per decade in the Beaufort Sea. The ORA MMM and EN4.2.0.g10 are also showing a more saline trend from the Nansen Basin

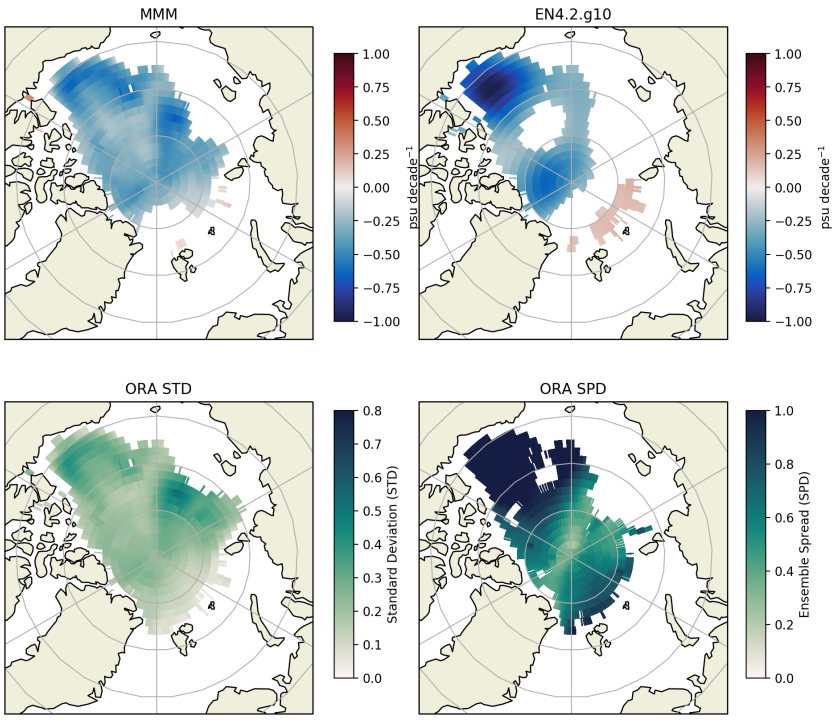

Figure 4.11: Salinity trends for the MMM and EN4.2.0.g10 and statistical analyses, ORA STD and ORA SPD, for the 0–100 m layer.

to the Fram Strait of up to 0.25 PSU per decade. The MMM trends are patchy for the area which is reflected in the ORA SPD that shows noise for the area.

The results for the 100–300 m layer can be seen in Figures 4.12 and 4.13. The ORA SPD shows strong disagreement and noise over the whole of the AO, but especially in the Fram Strait and Eurasian Basin. Hence, there is barely any significant trends for the area in the ORA MMM, but the ORA STD does show variations relative to time series mean of the magnitude 0.3 °C. Regardless, the ORA MMM does show a localised warming at the Fram Strait of 0.3 °C per decade. However, the EN4.2.g10 shows strong warming for the Eurasian Basin and central AO of similar magnitude as ORA MMM for the Fram Strait. At the Laptev Sea, the EN4.2.0.g10 shows a strong warming trend of 0.4 °C per decade. For the Eurasian Basin and parts of the Amerasian basin, both the MMM and EN4.2.0.g10 show salinifying trend of up to 0.2 PSU per decade (Figure 4.13). The ORA SPD, however, shows some noise for the Eurasian basin that strengthens toward the Nansen Basin and Fram Strait. On the contrary, at the Chukchi Sea toward the Beaufort Sea, both ORA MMM and EN4.2.0.g10 show a cooling trend of -0.2 °C per decade (Figure 4.12). For the same area, ORA MMM and EN4.2.g10 also show strong freshening trend of down to -0.4 PSU/decade while the ORAs seem to be in fairly good agreement for the center of the freshening trend (Figure 4.13).

The results for the layer 300–700 m are in Figures 4.14 and 4.15. The MMM

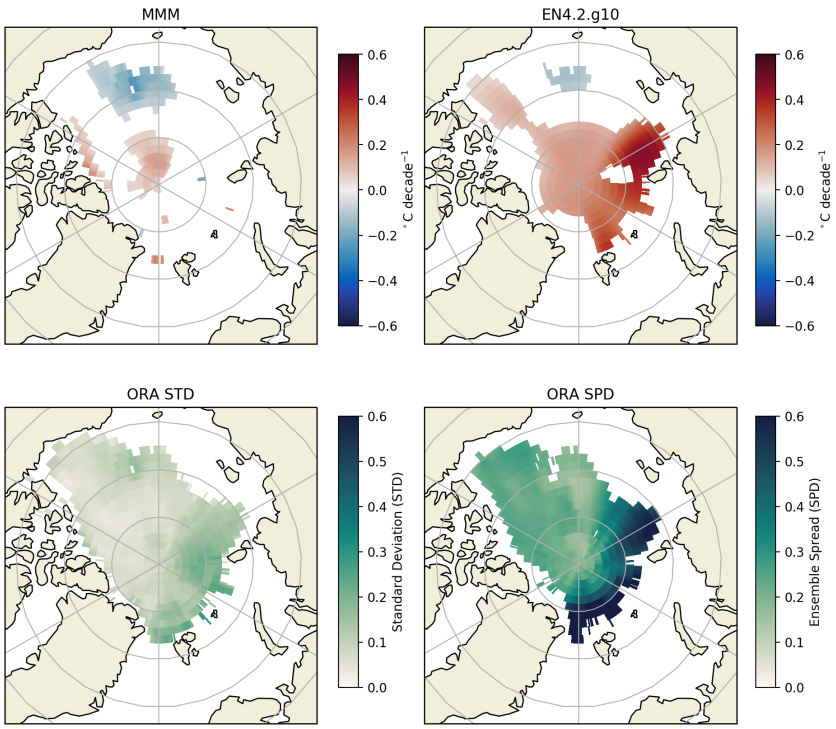

Figure 4.12: Temperature trends for the MMM and EN4.2.0.g10 and statistical analyses, ORA STD and ORA SPD, for the 100–300 m layer.

shows warming of 0.1 °C per decade from the central AO toward the Beaufort Sea. The EN4.2.0.g10 shows overall warming for the whole of the AO from 0.1 °C to 0.2 °C per decade, excluding the Siberian Shelf Seas and the Fram Strait. The ORA MMM, however, shows a warming of 0.3 °C for the Fram Strait and partly in the Kara and Barents Seas (Figure 4.14) coinciding with increasing trend in salinity of about 0.03 PSU/decade (Figure 4.15). The MMM also shows a cooling trend of -0.1 °C aligned with the Transpolar Drift (Figure 4.14), while also both MMM and EN4.2.g10 show a corresponding freshening trend (Figure 4.15). Overall, the salinity trends (Figure 4.15) are more variable and fragmented but both the MMM and EN4.2.0.g10 show increasing salinity in the Beaufort Sea, where the ORA STD is also large denoting changes. ORA SPD, however, shows strong disagreement amongst ORAs over the Amerasian Basin, with the only less noisy area being along the Transpolar Drift in the Eurasian Basin.

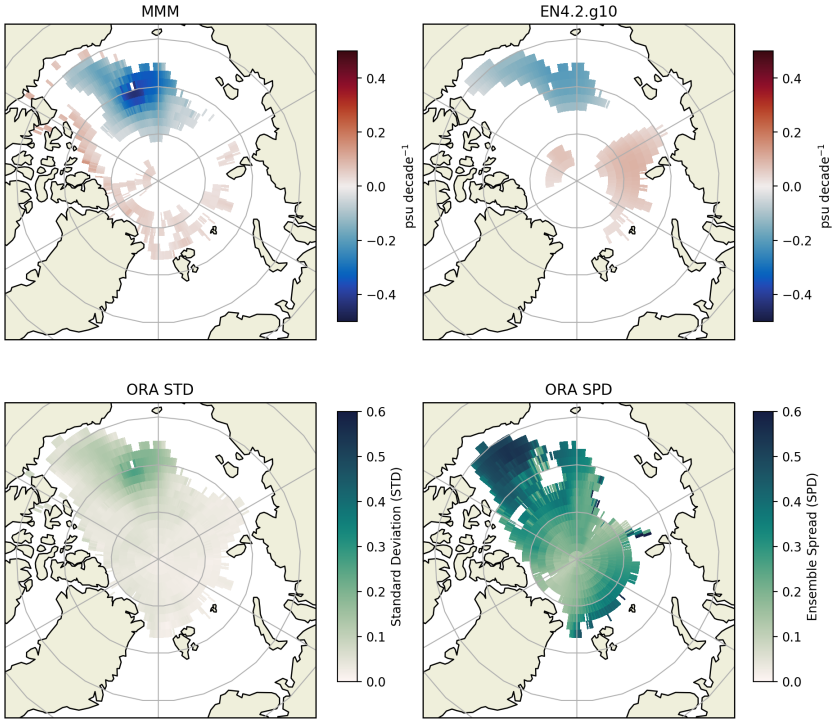

Figure 4.13: Salinity trends for the MMM and EN4.2.0.g10 and statistical analyses, ORA STD and ORA SPD, for the 100–300 m layer.

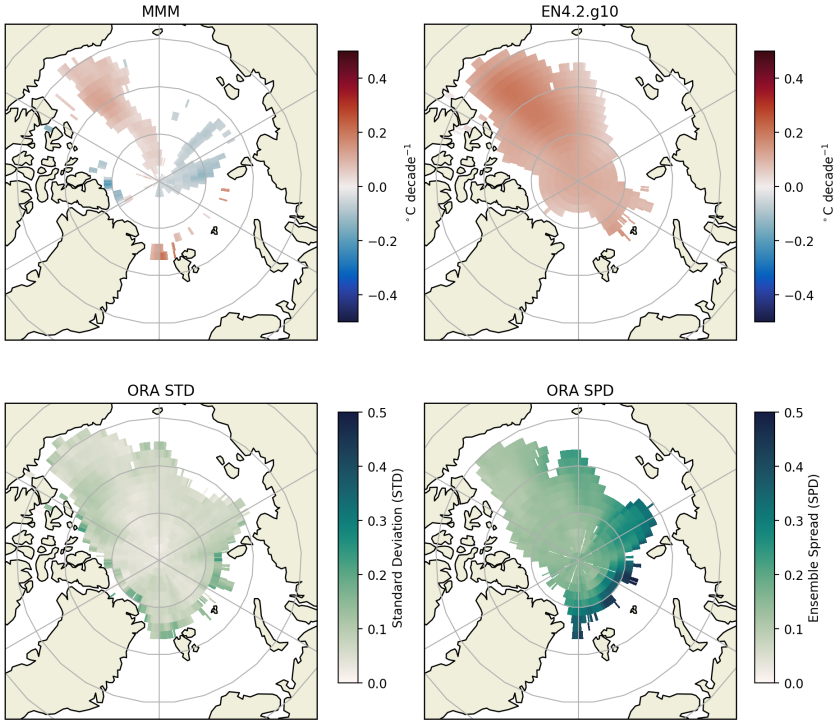

Figure 4.14: Temperature trends for the MMM and EN4.2.0.g10 and statistical analyses, ORA STD and ORA SPD, for the 300–700 m layer.

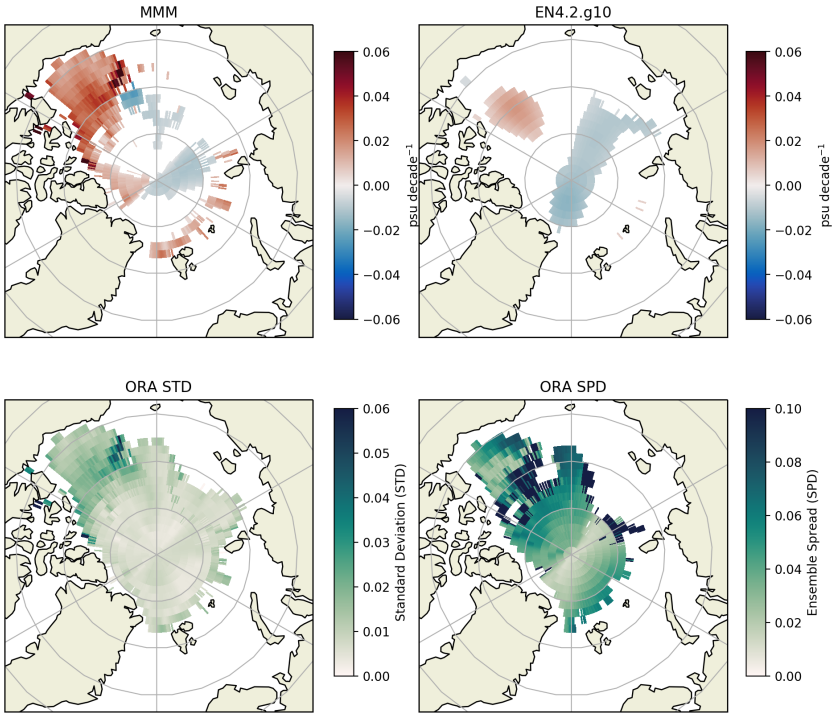

Figure 4.15: Salinity trends for the MMM and EN4.2.0.g10 for the MMM and EN4.2.0.g10 and statistical analyses, ORA STD and ORA SPD, for the 300–700 m layer.

5. Discussion

In this chapter the results from this thesis are summarised and discussed in light of literature and physical processes presented in Chapter 2. First the main findings based on the anomaly time series and basin-averaged trends are summarised. Then specific trends identified from the per grid products are selected and discussed in terms of literature and known dynamics. After the main findings, the trends are critically assessed and reflections on the reliability of the results are presented.

5.1 Main findings

Statistically significant trends were found for the AO. The anomaly time series showed variability over the years and across the ORAs, but the overall trends showed increasing OHC (°Cm) in the top 700 m in both Eurasian and Amerasian Basins, accompanied with freshening trends. The results were more variant when the AO was divided into layers, the top 0–100 m showed warming of 3 °Cm per decade in the Eurasian Basin with freshening of -2 PSUm per decade. For the Amerasian Basin, there was a strong freshening trend of -3.5 PSUm per decade. For the layer 100–300 m, the Eurasian basin was getting more saline (6 PSUm per decade) and the Amerasian Basin slightly fresher 0.6 PSUm per decade. For the layer 300–700 m, the salinity was found increasing in the Amerasian Basin (0.4 PSUm per decade).

5.1.1 Exceptionally warm year of 2007

During the study period, in year 2007, record breaking losses in summer sea ice were observed (Stroeve et al., 2008). The losses were caused by warm airmasses intruding the Arctic that persisted for three months (Serreze and Meier, 2018). Stroeve et al. (2008) noted that the skies were predominantly clear which resulted in stronger melt. The sea surface temperatures also increased (Stroeve et al., 2008). In the anomaly time series, warm peak was observed in both the Eurasian and Amerasian Basins (Figures 4.1; 4.3). Clear skies, lesser ice cover and persistent, strong winds could deepen the PML and allow for more heat to be absorbed by the PML resulting in the observed anomaly.

5.1.2 Warming and salinification of the Eurasian Basin

When examining the per grid trends, it became clear that for the Eurasian Basin temperatures increased across all layers, especially north of the Kara and Barents seas coinciding with increasing salinity, especially in 100–300m and 300–700 m layers. As the AW layer is located at 150 to 800 m depth in the Eurasian Basin and extends from the Fram Strait and the Barents Sea, the results along the flow pattern of the AW inflow suggest that the AW inflow is getting more warm and saline. This hypothesis is supported by the anomaly time series for the Fram Strait (Chapter 4, Figure 4.5) where a slight increasing trend was observed. Årthun et al. (2019) examined AW heat transport and found that even though the inflow to Barents Sea is weakening, its heat content is increasing. Furthermore, Polyakov et al. (2017) found that the total heat content of AW has increased and its role in the Arctic climate will likely increase as the stratification weakens and more heat could be released up from the warm AW layer. They suggest that the enhanced release of heat would be one of the causes in recent sea ice declines in the eastern Eurasian Basin. However, as the surface warming here is extended uniformly from the Nansen Basin to north of the Chukchi Sea, it is more likely that the 0–100 m results here reflect the additional atmospheric heat uptake of the PML during summer, allowed for by the reduced summer extend of sea ice, than increases in upward heat fluxes from the warmer AW layer.

5.1.3 Cooling of the Fram Strait 0-100 m

The per grid trends revealed cooling of the Fram Strait for the top layer of 0–100 m. The anticyclonic circulation in the Amerasian Basin and the cyclonic circulation in the Eurasian Basin converge to form the Transpolar Drift that flows the surface waters of both basins (mainly in the Eurasian Basin) toward the Fram Strait, exporting sea ice out of the AO (see Figure 5.1). Towards the end of the study period (year 2007), northern winds were strengthened and the ice export via the Fram Strait increased (Serreze and Meier, 2018). Furthermore, IPCC (2019) reported that the sea ice drift speed has increased and more ice is being transported from the AO. This increasing export of ice via the Fram Strait could play a role in the observed cooling in the outflow branch of the Fram Strait.

It has been suggested that the ORAs over-estimate sea ice drift velocities (Chevallier et al., 2017) but as the cooling trend was also observed in EN4.2.0.g10, it is more likely that the cooling observed here is inherent to observations than increased sea ice drift velocity bias. Furthermore, as more heat is absorbed by the PML due to lesser summer sea ice extent, the onset of freezing is delayed. This leads to thinner sea ice, which in turn breaks easier under wind forcing, exposing the AO surface to further solar heating (Cottier et al., 2016). This strongly connects the sea ice processes to the previously observed warming of the 0–100 m layer from the Nansen Basin to north of the Chukchi

Sea.

5.1.4 Freshening of the Beaufort Sea

The Amerasian Basin was found freshening down to -0.5 PSU per decade in the top 300 m in the Beaufort Sea. These results compare well with the magnitude of freshening of the Beaufort Sea noted in previous studies (e.g. IPCC, 2019; Carmack et al., 2016). IPCC (2019) reported that the freshwater inflow via the Bering Strait has increased by 30 km^3yr^{-1} while the river inflow has also increased. From the ice velocity patterns and freshwater content in Figure 5.1, it can be seen that the Beaufort Gyre (BG) has anticyclonic circulation that accumulates freshwater in its center. The freshwater sources from seasonal ice melt, the Pacific inflow, Arctic rivers and also meltwater from Greenland (Carmack et al., 2016).

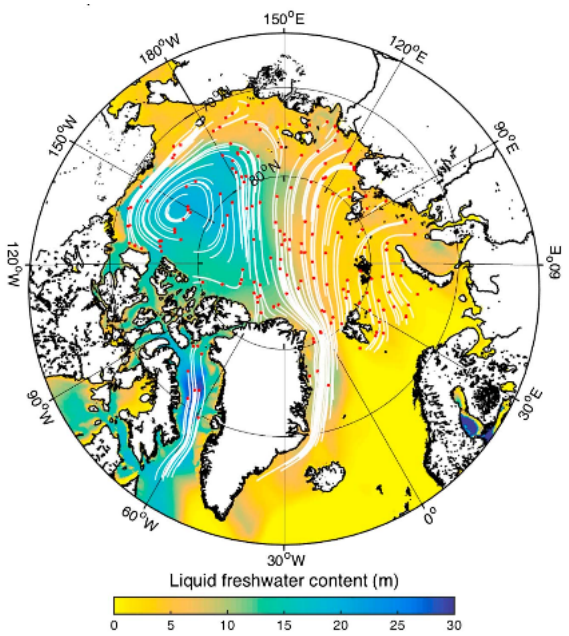

Figure 5.1: Freshwater accumulation and ice velocities. Source: Carmack et al. (2016).

Giles et al. (2012) found that the storage of freshwater in the BG varies with the wind stress curl and proposed Ekman pumping as the main cause for accumulation and redistribution of freshwater in the BG. Ekman pumping is prominent in the BG due to the Arctic High anticyclonic circulation that is centered in the BG (Proshutinsky et al., 2009). When the anticyclonic forcing weakens, the freshwater is released (Proshutinsky et al., 2009). Over most of the study period (from 1997), anticyclonic winds dominated over the BG (Proshutinsky et al., 2012). Ekman pumping alongside the diminishing summer sea ice in the Beaufort Sea (IPCC, 2019), most likely caused the -0.5 PSU per decade trend observed in the Beaufort Sea. Accompanied with the increases in salinity observed in

the Eurasian Basin, some of the freshening observed in the BG could also be freshwater transported from the Eurasian Basin.

5.1.5 Other changes in the Amerasian Basin

There has been observations on the warming of the surface layer at the Beaufort Sea (e.g. Bourgain and Gascard, 2012; Lique and Steele, 2013), that was not captured by the ORA MMM. Bourgain and Gascard (2012) examined hydrological data in the AO and found warming of the PW inflow between 1997 and 2008, consequently causing warming in the Beaufort Sea surface layer. This has been proposed to be one of the causes for the loss of sea ice in the Beaufort Sea (Bourgain and Gascard, 2012; Lique and Steele, 2013; IPCC, 2019). The ORA SPD revealed that the ORAs were in disagreement on the temperature trends in the Beaufort Sea. As the observational product EN4.2.0.g10 showed strong warming trend in the area, it is likely that the ORA MMM's lack of trend is due to model or assimilation aspects. On closer inspection most of the ORAs showed warming in the area but in particular SODA3.3.1 and TOPAZ4 showed strong cooling trends (Appendix A, Figure A.1).

Moreover, in the Amerasian Basin, the 100–300 m layer showed freshening and cooling north of the Chukchi Sea. This freshening and cooling of the halocline is the opposite to the trend observed in the Eurasian basin that was strongly getting warmer and more saline. The freshening trend is most likely due to observed freshening of the PW inflow, that is then pumped to the ocean interior at the Chukchi Sea. The cooling trend accompanying the freshening could suggest that the PW is able to reach deeper into the ocean interior at the Chukchi Sea than previously due to for example enhanced mixing and/or Ekman pumping allowed for by the losses of sea ice observed at the Chukchi Sea during summer.

Furthermore, the dynamics determining the Amerasian Basin hydrography are complicated. Proshutinsky et al. (2011) stated that the exact pathways of PW are not known due to lack of observations. They also found significant discrepancies between models in handling the PW route and also the thickness of the PW layer. As the Beaufort Sea warming has been attributed to warming of the PW inflow, this is likely the cause of the disagreement of ORAs in the area. Furthermore, the ORAs disagreed on the location of the maximum surface layer freshening trend at the BG. This could result, for example, from differing wind forcing driving different circulation patterns shifting the location where the BG build up of freshwater occurs.

5.1.6 AW path dominating changes in the 300–700 m layer

For the 300–700 m layer occupied by the AW, the Barents Sea was warming and getting more saline, while along the Lomonosov Ridge waters were cooling (down to -0.1 °C decade^{-1}) and freshening (down to -0.02 PSU decade^{-1}). This suggests that the AW flow is mainly from the Barents Sea toward the Amerasian Basin during the study period, as the Amerasian Basin was also warming (up to 0.1 °C decade^{-1}) and getting more saline (up to 0.05 PSU decade^{-1}) at this depth.

5.2 Trends or natural variability

As the anomaly time series showed a lot of variability over the years, it raises a question whether or not the results presented in this thesis are in fact trends or just natural variability. In the AO especially, it is very difficult to separate warming trends linked to climate change due to variability that may occur in decadal or even longer timescales (Lique and Steele, 2013). For example, linkages between the North Atlantic Oscillation (NAO) and sea ice variability, and NAO index and AW inflow have been found (Caian et al., 2018; Ilicak et al., 2016). The study period here, 17 years, is a long enough time period to catch some variability in the AO, caused for example by NAO, but not long enough to embrace, for example, the 11-year solar cycle, or other longer timescale forcings. For instance, Roy (2018) proposed solar cycles to have some influence on the recent sea ice decline in the Arctic. Furthermore, the freshening trend at BG was partly attributed to the Arctic High, strength of which could have a cyclic behaviour.

Furthermore, many publications have indicated changes and variations in the AW inflow (Lique and Steele, 2013). Indeed, Bourgain and Gascard (2012) did not find a warming trend in the AW inflow outside of natural variability between 1997 and 2008, contradictory to findings in this study and others (e.g. IPCC, 2019). Polyakov et al. (2004) examined 100 years long hydrological record for the AO and found that during the 20th century, the AW variability had low-frequency oscillations from 50 to 80 years. The record captured warming and salinification of the AW layer over the recent decades but the temperature trend also showed variability, and the short-term trends were found to be strongly amplified by multidecadal variations (Polyakov et al., 2004).

Although caution must be taken when observing trends in data sets with limited observations and time scale, the trends observed in this study have continued, if not even accelerated, to date (e.g. IPCC, 2019) which suggests the trends are outside of natural variability and could be linked to global climate change.

5.3 Reliability of the results

5.3.1 Comparing to EN4.2.0.g10

Assessing errors in the trends presented by the ORA MMM is difficult due to lack of reality to compare the results to. The MMM was compared to the observational product EN4.2.0.g10 and they were found to compliment each other fairly well at times. However, using a statistical reanalysis for the comparison does not give indication of the absolute truth. Masina et al. (2017) emphasized that the observation-methods are highly dependent on the gap-filling methods, which can cause biases in the trends observed here. Furthermore, many have stated that ORAs are perhaps more physically realistic than observation-only products (e.g. Balmaseda et al., 2015; Uotila et al., 2018) as the inclusion of the model physics can fill in the gaps between measurements more realistically than any statistical method could. That being said, the models also suffer from inaccuracies due to their reduced resolutions, and the assumptions and parametrisations they include.

Acknowledging the limitations of this comparison, the EN4.2.0.g10 and ORA MMM did show differences in their trends. Generally, the EN4.2.0.g10 showed stronger trends in the top 100 meters in both the Eurasian and Amerasian Basins, with stronger warming north of the Barents Sea and stronger cooling at the outflow branch of the Fram Strait. This was also noted in the ORA mean state study by Uotila et al. (2018) where they observed that the ORAs were on a lower side of oceanic heat transport towards the Arctic and that the EN4.2.g10 showed a warmer Barents Sea than the ORA MMM. Furthermore, Allison et al. (2019) noted that paucity of observations has been suggested to be a cause for long-term trends in OHC to be biased low spatially.

5.3.2 The ensemble method

The ensemble method worked well in this study as the extremities of singular ORAs were cancelled out and the ORA MMM was able to present similar trends to observations. ORA SPD revealed areas where the ORAs disagreed the most, namely the Fram Strait and Beaufort Sea. As discussed earlier, the ORAs were in disagreement with temperature trends in the Beaufort Sea which was probably due to the lack of observations on the PW inflow and the model physics varying on the PW flow routes. Furthermore, Steiner et al. (2004) identified disparities in presentation of AW temperature and transports across the Fram Strait as short-comings of ocean models in the AO. These could be some of the reasons why the ORAs were in disagreement at the Beaufort Sea and Fram Strait. Special consideration should be placed on the dynamics of these two areas and the inflows

in future research in the AO both in terms of measurements and model development.

Moreover, the results presented in this study can suffer from errors resulting from multiple steps on the way. Although the ensemble approach is able to dampen the extremities of individual ORAs, it assumes that all of the ORAs suffer from the same level of error or correctness. This is not always true. For example, ECDA3 was excluded from the ORA MMM in this study due to large areas of missing data in the AO which affected the data analysis and corrupted the statistical analyses. Furthermore, TOPAZ4 has been found to perform better in retrieving surface variables and its performance decreased with depth (Xie et al., 2017). In the results of this study, it was also noted that TOPAZ4 was an outlier at the deeper depth layers, for example in 300–700 m layer results presented in Figures 4.7 and 4.8, the deviance from the ORA MMM was even more pronounced in the per grid trends. However, simply being an outlier does not indicate that the ORA is more in the wrong. Although inter-comparisons are useful in estimating past changes, it is difficult to assess whether some ORAs are more accurate than others (Allison et al., 2019). Furthermore, as many of the key processes in the AO are parametrisised, such as convection, it is fair to assume that some of the ORAs are more correct in their choice of parametrisations than others. That correctness, however, can be cancelled out by choices on surface forcings and so on, eventually leading to somewhat similar level of correctness, or wrongness.

Even if the assumption of the same level of correctness holds, the ORAs can all suffer from same biases (Allison et al., 2019). These biases can result for example from the assimilated observations, forcing methods, model configurations and data assimilation methods. Especially as the measurements are scarce in the AO, the representativeness of the available observations and assimilation methods have a more crucial role than in the areas where measurements are available in larger quantities and at finer spatial resolution. The measurements in the AO get sparser with increasing depth. Hence, the reliability of the trends presented here decrease with increasing depth, especially in terms of salinity. This was also visible in the results of this thesis, as the depth increased the trends and anomalies became less coherent while the ORAs were disagreeing more. As a result, the trends for the layers 700–1500 m and 1500–3000 m layers were excluded from this study. Although the expansion of the Argo network has resulted into more data being available for the AO, more measurements especially at deeper depths are still needed to improve the ORAs. The deep ocean dynamics are also closely linked to the bottom topography via small-scale friction and hence, the resolution of the model can inhibit the accurate representation of the bottom friction. Furthermore, many important processes in the deep ocean are parametrisised, such as tides, bottom boundary layer and mixing, which partly explains the deviations of ORAs from each other as the choices on those parametrisations vary and are reflected on the output. Furthermore, as the observations in the deep ocean

are sparse, more weight relies on the reliability of these parametrisations, observations and assimilation methods. Improvements in the inclusion of the deep ocean physics is therefore encouraged. As these improvements come alongside increasing computational capacity, trend analysis in the deeper parts of the AO could also be achieved. Until then, the ORA MMM appears as a viable method for examining trends in the AO within the top 700 meters.

Moreover, the AO hydrography is closely linked with the sea ice dynamics. As the observations on sea ice volume and thickness are very sparse in the AO, much of the responsibility falls on the sea ice model used in the ORA in representing them (Chevallier et al., 2017). Chevallier et al. (2017) performed inter-comparison of sea ice-ocean dynamics in ORAs and found a large spread in their sea ice thickness and spatial distributions of volume. Too thin sea ice can for example result in the ice breaking too easily under wind forcing and lead to over estimations of ice drift (Chevallier et al., 2017), which could encourage new ice formation increasing the salinity in the surface layer which induces too enhanced mixing, and openings increase heat venting out of the AO. The ORAs also varied in their simulation of snow cover (Chevallier et al., 2017) which in terms of heat flux through the ice, is of importance to AO surface hydrography. Furthermore, the Marginal Ice Zone (MIZ) is a region of ice breaking and enhanced Ekman pumping (Kim et al., 2017). The location of the Ekman pumping varies with the ice edge (Kim et al., 2017) and the accurate presentation of the MIZ by the ORAs requires well established sea ice thickness. Therefore, more systematic sea ice thickness measurements are needed for more accurate analysis and in the meanwhile the focus should be on improving the assimilation of sea ice thickness to improve the performance of the ORAs in the AO (Chevallier et al., 2017).

5.4 Towards the new Arctic

If the observed changes in the hydrography and sea ice extent and thickness continue, the dynamics of the AO could be shifting to a new regime. Namely the decreasing sea ice extend could result in an increased transfer of momentum between the atmosphere and the AO which in turn could result in greater surface and internal wave energies. Therefore, wind driven mixing and turbulence are likely to take a greater role in the AO than seen in previous studies. Also more heat would be absorbed by the AO during summer months and the new mixing regime would likely mix the heat more efficiently. Currently, temperature is a passive tracer in the AO leaving the ocean dynamics relying on the salinity field (Timmermans and Jayne, 2016). As the AO warms up, new dynamical balances are to be expected as the temperature will play a greater role than previously, which in turn could further change the mixing regime of the interior of the AO (Timmermans and

Jayne, 2016). Although this is highly speculative, the fact remains that we do not know how the AO hydrography and dynamics will shape as we are moving towards the new Arctic, which makes further reviewing and improvement of the aforementioned measurement, assimilation and model short-comings exceedingly important.

6. Conclusions

The results of this study indicate that the AO is indeed under change, as statistically significant trends were found for the AO. The Eurasian Basin was found to be warming across all layers (up to 0.3°C decade^{-1}) accompanied by salinification, except for localised cooling in the top 100 meters in the western basin, near the Fram Strait (-0.2°C decade^{-1}). This indicates additional heat uptake by the surface layer of 0–100 meters and also increasing heat and salinity content of the AW inflow, while the transport of sea ice out of the AO has increased. The Amerasian Basin, on the other hand, showed a strong freshening trend culminating at the Beaufort Gyre. This is most likely due to the anticyclonic wind forcing and increasing freshwater inflow to the Beaufort Sea. The Amerasian Basin also showed a warming trend in the 300–700 m layers but a cooling trend in the 100–300 m layer north of the Chukchi Sea. As a result, it seems that the AH is getting stronger in the Amerasian Basin and weakening in the Eurasian Basin.

The ORA output varied significantly but the extremities of singular ORAs were cancelled out by the ensemble method. The ensemble spread identified areas where more improvements are needed in representing the AO, including the Fram Strait, Beaufort Sea and AW and PW layers. The trends presented by the ORA MMM reflected previous observations published in literature. This suggests that the ORA MMM is a viable method for studying the changes in the AO where the lack of measurements hinders the studying of oceanic change, if taken in consideration its limitations. The ORA MMM was not successful at retrieving reliable trends for the layers deeper than 700 m as the ORAs disagreed more with increasing depth. Reviewing the performance of ORAs and ocean models at depths deeper than 700 m is important in order to identify sources of error in the model configurations and parametrisations in presenting deeper oceans. Today, the reviewing is still hindered due to paucity of measurements but as the measurement network expands and ORAs are updated as the methods, parametrisations and computational capacities improve, assessment of the deeper AO can be achieved. All in all, ORAs, especially the ORA ensemble, shows true potential in climate change studies in the AO.

Acknowledgements

This thesis was funded by the Institute for Atmospheric and Earth System Research (INAR).

First and foremost, I would like to thank my supervisor Petteri Uotila for his guidance and support throughout this thesis. His passion and insight to the field is very inspiring while his dedication to his students has been admirable and unparalleled. I have enjoyed our many conversations and always left feeling inspired. Thank you for seeing the potential in me and taking me in as a summer worker back in 2018. Thank you also to Ekaterina Ezhova, for reviewing this thesis and providing me with a lot of very useful feedback that truly improved this thesis.

I also acknowledge and thank the Ocean Reanalyses Intercomparison Project (ORA-IP) for producing and making available their Ocean Reanalysis outputs and the Integrated Climate Data Center (ICDC) at Hamburg University for archiving the data and providing access.

I would also like to take this opportunity to thank Laura Tuomi and Lauri Laakso from Finnish Meteorological Institution for taking me in their respective research groups, guiding me and also being very understanding on the delay of this thesis. Through working in their research groups I have met inspiring researchers and had opportunities I otherwise would not have had. That being said, I was very lucky to have professor Igor Polyakov as a visiting professor at the Finnish Meteorological Institution while I was working on this thesis. I would like to thank him for the insights he provided me with.

I would also like to thank Jani Strömberg, Joula Siponen and Joonatan Ala-Könni for the summer 2018 and for the friendships that ensued. They provided me with both technical and moral support throughout my thesis. Thank you also belongs to Hanna Berg for the moral support through my MSc studies and beyond.

My final thanks goes to my dear family and friends for all their love and support. Thank you Seija, Kimmo, Jaakko and Maisa for being there for me, always and unconditionally. Special mention also to Veera and Mena for all the conversations we have had throughout the years. Thank you also to everyone who I have not mentioned but has been there for me. I feel very grateful to have family and friends who keep reminding me of my capabilities whenever I start to doubt myself.

Bibliography

Adcroft, A., Campin, J.-M., Doddridge, E., Dutkiewicz, S., Evangelinos, C., Ferreira, D., Follows, M., Forget, G., Fox-Kemper, B., Heimbach, P., Hill, C., Hill, E., Hill, H., Jahn, O., Klymak, J., Losch, M., Marshall, J., Maze, G., Mazloff, M., Menemenlis, D., Molod, A., and Scott, J. (2019). Welcome to mitgcm's user manual.

Aksenov, Y., Bacon, S., Coward, A., and Nurser, G. (2010). The north atlantic inflow to the arctic ocean: High-resolution model study. *Journal of Marine Systems*, 79(1–2):1–22.

Aksenov, Y., Karcher, M., Proshutinsky, A., Gerdes, R., de Cuevas, B., Golubeva, E., Kauker, F., Nguyen, A. T., Platov, G. A., Wadley, M., Watanabe, E., Coward, A. C., and Nurser, A. J. (2016). Arctic pathways of pacific water: Arctic ocean model intercomparison experiment. *JGR Oceans*, 121(1):27–59.

Allison, L., Roberts, C., Palmer, M., Hermanson, L., Killick, R., Rayner, N., Smith, D., and Andrews, M. (2019). Towards quantifying uncertainty in ocean heat content changes using synthetic profiles. *Environmental Research Letters*, 14(8):084037.

Årthun, M., Eldevik, T., and Smedsrud, L. (2019). The role of atlantic heat transport in future arctic winter sea ice loss. *Journal of Climate*, 32(11):3327–3341.

Balmaseda, M., Hernandez, F., Storto, A., Palmer, M., Alves, O., Shi, L., Smith, G., Toyoda, T., Valdivieso, M., Barnier, B., Behringer, D., Boyer, T., Chang, Y.-S., Chepurin, G., Ferry, N., Forget, G., Fujii, Y., Good, S., Guinehut, S., Haines, K., Ishikawa, Y., Keeley, S., Köhl, A., Lee, T., Martin, M., Masina, S., Masuda, S., Meyssignac, B., Mongensen, K., Parent, L., Peterson, K., Tang, Y., Yin, Y., Vernieres, G., Wang, X., Waters, J., Wedd, R., Wang, O., Xue, Y., Chevallier, M., Lemieux, J.-F., Dupont, F., Kuragano, Y., Kamachi, M., Awaji, T., Caltabiano, A., Wilmer-Becker, K., and Gaillard, F. (2015). The ocean reanalyses intercomparison project (ora-ip). *Journal of Operational Oceanography*, 8(S1):s80–s97.

Blockley, E., Lea, D., Martin, M., McLaren, A., Mirouze, I., Ryan, A., Siddorn, J., Storkey, D., and Waters, J. (2014a). Recent development and assessment of the met

office operational global ocean forecasting system (foam). In Buch, E., Antoniou, Y., Eparkhina, D., and Nolan, G., editors, *Operational oceanography for sustainable blue growth*. Proceedings of the seventh EuroGOOS international conference, Lisbon, Portugal.

Blockley, E., Martin, M., McLaren, A., Ryan, A., Waters, J., Lea, D., Mirouze, I., Peterson, K., Sellar, A., and Storkey, D. (2014b). Recent development of the met office operational ocean forecasting system: an overview and assessment of the new global foam forecasts. *Geosci Model Dev*, 7(6):2613–2638.

Bourgain, P. and Gascard, J. (2011). The arctic ocean halocline and its interannual variability from 1997 to 2008. *Deep-Sea Research I*, 58:745–756.

Bourgain, P. and Gascard, J. (2012). The atlantic and summer pacific waters variability in the arctic ocean from 1997 to 2008. *Geophysical Research Letters*, 39(L05603):1–6.

Brodeau, L., Barnier, B., Tréguier, A.-M., Penduff, T., and Gulev, S. (2009). An era40-based atmospheric forcing for global ocean circulation model. *Ocean Modelling*, 31(3–4):88–104.

Caian, M., Koenigk, T., Döscher, R., and Devasthale, A. (2018). An interannual link between arctic sea-ice cover and the north atlantic oscillation. *Clim Dyn*, 50:423–441.

Carmack, E., Polyakov, I., Padman, L., Fer, I., Hunke, E., Hutchings, J., Jackson, J., Kelley, D., Kwok, R., Layton, C., Melling, H., Perovich, D., Persson, O., Ruddick, B., Timmermans, M.-L., Toole, J., Ross, T., Vavrus, S., and Winsor, P. (2015). Toward quantifying the increasing role of oceanic heat in sea ice loss in the new arctic. *Bulletin of the American Meteorological Society*, pages 2079–2105.

Carmack, E., Yamamoto-Kawai, M., Haine, T., Bacon, S., Bluhm, B., Lique, C., Melling, H., Polyakov, I., Straneo, F., Timmermans, M.-L., and Williams, W. (2016). Freshwater and its role in the arctic marine system: Sources, disposition, storage, export, and physical and biogeochemical consequences in the arctic and global oceans. *J. Geophys. Res. Biogeosci.*, 121:675–717.

Carton, J. and Giese, B. (2010). A reanalysis of ocean climate using simple ocean data assimilation (soda). *Monthly Weather Review*, 136(8):2999–3017.

Chang, Y.-S., Zhang, S., Rosati, A., Delworth, T., and Stern, W. (2013). An assessment of oceanic variability for 1960-2010 from the gfdl ensemble coupled data assimilation. *Clim Dyn*, 40(3–4):775–803.

Chevallier, M., Smith, G. C., Dupont, F., Lemieux, J.-F., Forget, G., Fujii, Y., Hernandez, F., Msadek, R., Peterson, K. A., Storto, A., Toyoda, T., Valdivieso, M., Vernieres, G., Zuo, H., Balmaseda, M., Chang, Y.-S., Ferry, N., Garric, G., Haines, K., Keeley, S., Kovach, R. M., Kuragano, T., Masina, S., Tang, Y., Tsujino, H., and Wang, X. (2017). Intercomparison of the arctic sea ice cover in global ocean–sea ice reanalyses from the ora-ip project. *Climate Dynamics*, 49(3):1107–1136.

Cottier, F., Steele, M., and Nilsen, F. (2016). Sea ice and arctic ocean oceanography. In Thomas, D., editor, *Sea ice*, pages 197–215. Wiley, Chichester.

Curry, J. and Schramm, J. (1995). Sea ice-albedo climate feedback mechanism. *Journal of Climate*, 8:240–247.

Cushman-Roisin, B. (1994). *Introduction to Geophysical Fluid Dynamics*. Academic Press.

Destin, C. (2014). The argo revolution. https://www.climate.gov/news-features/features/argo-revolution. Accessed: 17/02/2020.

Dosser, H., Rainville, L., and Toole, J. (2013). Near-inertial internal wave field in the canada basin from ice-tethered profilers. *J. Phys. Oceanogr.*, 44(413426).

Doucette, J. (2018). Arctic halocline. https://www.whoi.edu/multimedia/arctic-halocline/. Accessed: 17/02/2020.

ECMWF (2019). Ocean reanalysis/analysis. https://www.ecmwf.int/en/research/climate-reanalysis/ocean-reanalysis. Accessed: 17/02/2020.

Evensen, G. (2003). The ensemble kalman filter: theoretical formulation and practical implementation. *Ocean Dynamics*, 53:343–367.

Fahrbach, E., Meincke, J., Osterhus, S., Rohardt, G., Schauer, U., Tverberg, V., and Verduin, J. (2001). Direct measurements of volume transports through fram strait. *Polar Res*, 20:217–224.

Fichefet, T. and Maqueda, M. A. M. (1997). Sensitivity of a global sea ice model to the treatment of ice thermodynamics and dynamics. *Journal of Geophysical Research: Oceans*, 102(C6):12609–12646.

Fox-Kemper, B., Adcroft, A., Böning, C. W., Chassignet, E. P., Curchitser, E., Danabasoglu, G., Eden, C., England, M. H., Gerdes, R., Greatbatch, R. J., Griffies, S. M., Hallberg, R. W., Hanert, E., Heimbach, P., Hewitt, H. T., Hill, C. N., Komuro, Y., Legg, S., Le Sommer, J., Masina, S., Marsland, S. J., Penny, S. G., Qiao, F., Ringler, T. D., Treguier, A. M., Tsujino, H., Uotila, P., and Yeager, S. G. (2019). Challenges and prospects in ocean circulation models. *Frontiers in Marine Science*, 6:65.

Garric, G., Parent, L., Greiner, E., Drévillon, M., Hamon, M., Lellouch, J., Régnier, C., Desportes, C., Le Galloudec, O., Bricaud, C., Drillet, Y., Hernandez, F., Dubois, C., and P.-Y., L. T. (2018). Performance and quality assessment of the global ocean eddy-permitting physical reanalysis glorys2v4. In Buch E, Fernandez V, N. G. E. D., editor, *Operational oceanography serving sustainable marine development.* Proceedings of the eight EuroGOOS international conference, Bergen, Norway.

Giles, K., Laxon, S., Ridout, A., Wingham, D., and Bacon, S. (2012). Western arctic ocean freshwater storage increased by wind-driven spin-up of the beaufort gyre. *NATURE GEOSCIENCE*, 5(3):194–197.

Good, S. A., Martin, M., and Rayner, N. (2013). En4: quality controlled ocean temperature and salinity profiles and monthly objective analyses with uncertainty estimates. *Journal of Geophysical Research: Oceans*, 118:6704–6716.

Goosse, H., Deleersnijder, E., Fichefet, T., and England, M. (1999). Sensitivity of a global coupled ocean-sea ice model to the parameterization of vertical mixing. *J. Geophys. Res*, 104(13):681–695.

Griffies, S. (2004). *Fundamentals of ocean climate models*. Princeton University Press.

Griffies, S., Böning, C., Bryan, F., Chassignet, E., Gerdes, R., Hasumi, H., Hirst, A., Treguier, A., and Webb, D. (2000). Developments in ocean climate modelling. *Ocean Modell*, 2:123–192.

Griffies, S. M., Biastoch, A., Böning, C., Bryan, F., Danabasoglu, G., Chassignet, E. P., England, M. H., Gerdes, R., Haak, H., Hallberg, R. W., Hazeleger, W., Jungclaus, J., Large, W. G., Madec, G., Pirani, A., Samuels, B. L., Scheinert, M., Gupta, A. S., Severijns, C. A., Simmons, H. L., Treguier, A. M., Winton, M., Yeager, S., and Yin, J. (2009). Coordinated ocean-ice reference experiments (cores). *Ocean Modelling*, 26(1):1–46.

Hartmann, D. (2016). The energy balance of the surface. In *Global Physical Climatology*, pages 95–130. Elsevier Science, Seattle, the US.

Holland, M., Bitz, C., and Tremblay, B. (2006). Future abrupt reductions in the summer arctic sea ice. *Geophys. Res. Lett.*, 33(23):1–5.

Holloway, A. and Proshutinsky, G. (2007). Role of tides in arctic ocean/ice climate. *Journal of Geophysical Research*, pages 1–10.

Houtekamer, P. and Mitchell, H. (1997). Data assimilation using an ensemble kalman filter technique. *Monthly Weather Review*, 126:796–811.

Hunke, E., Lipscomb, W., Turner, A., Jeffery, N., and Elliott, S. (2015). *CICE: The Los Alamos Sea Ice Model. Documentation and Software User's Manual. Version 5.1.* T-3 Fluid Dynamics Group, Los Alamos National Laboratory, Tech. Rep. LA-CC-06-012.

Hunke, E. C. and Dukowicz, J. K. (1997). An elastic-viscous-plastic model for sea ice dynamics. *Journal of Physical Oceanography*, 27:1849–1867.

Ilicak, M., Drange, H., Wang, Q., Gerdes, R., Aksenov, Y., Bailey, D., Bentsen, M., Biastoch, A., Bozec, A., Böning, C., Cassou, C., Chassignet, E., Coward, A., Curry, B., Danabasoglu, G., and Danilov, S. (2016). An assessment of the arctic ocean in a suite of interannual core-ii simulations. part iii: Hydrography and fluxes. *Ocean Modelling*, 100:141–161.

IOC, SCOR, and IAPSO (2010). *The international thermodynamic equation of seawater - 2010: Calculation and use of thermodynamic properties.* Intergovernmental Oceanographic Commission, Manuals and Guides No. 56, UNESCO.

IPCC (2013). *Climate Change 2013: The Physical Science Basis.* Cambridge University Press, Cambridge, United Kingdom and New York, NY, USA.

IPCC (2019). *Special Report on the Ocean and Cryosphere in a Changing Climate.* Cambridge University Press.

Kantha, L. and Clayson, C. (2000). *Numerical Models of Oceans and Oceanic Processes.* Academic Press, USA, California.

Kim, T., Ha, H., Wåhlin, A., Lee, S., Kim, C., Lee, J., and Cho, Y. (2017). Is ekman pumping responsible for the seasonal variation of warm circumpolar deep water in the amundsen sea? *Continental Shelf Research*, 132:38–48.

King, H. (2017). Arctic ocean seafloor features map. https://geology.com/articles/arctic-ocean-features/. Accessed: 17/02/2020.

Köhl, A. (2015). Evaluation of the gecco2 ocean synthesis: Transports of volume, heat and freshwater in the atlantic. *Q. J. R. Met. Soc*, 141(686):166–181.

Lammers, R., Shiklomanov, A., Vörösmarty, C., Fekete, B., and Peterson, B. (2001). Assessment of contemporary arctic river runoff based on observational discharge records. *Journal of Geophysical Research*, 106(D4):3321–3334.

Large, W., McWilliams, J., and Doney, S. (1994). Oceanic vertical mixing: a review and a model with a nonlocal boundary layer parameterization. *Reviews of Geophysics*, 32(4):363–403.

Large, W. G. and Yeager, S. (2004). *Diurnal to decadal global forcing for ocean and sea-ice models: the data sets and flux climatologies*. NCAR Technical Note, CGD Division of the National Center for Atmospheric Research.

Lee, C., Cole, S., Doble, M., Freitag, L., Hwang, P., Jayne, S., Jeffries, M., Krishfield, R., Maksym, T., Maslowski, W., Owens, B., Posey, P., Rainville, L., Shaw, P., Stanton, T., Thomson, J., Timmermans, M.-L., Toole, J., Wadhams, P., Wilkinson, J., and Zhang, Z. (2012). *A global ocean model with double-diffusive mixing.* Marginal Ice Zone (MIZ) Program: Science and Experiment Plan, Technical Report APL-UW 1201, Applied Physics Laboratory, University of Washington, Seattle.

Lique, C. and Steele, M. (2013). Seasonal to decadal variability of arctic ocean heat content: A model-based analysis and implications for autonomous observing systems. *JGR Oceans*, 118(4):1673–1695.

Madec, G., Bourdalle-Badie, R., Bouttier, P.-A., Bricaud, C., Bruciaferri, C., C., D., Chanut, J., Clementi, E., Coward, A., Delgrosso, D., Ethe, J., Flavoni, S., Graham, T., Harle, J., Iovino, D., Lea, D., Levy, C., Lovato, T., Martin, N., Masson, S., Mocavero, S., Paul, J., Rousset, C., Storkey, D., Storto, A., and Vancoppenolle, M. (2017). Nemo ocean engine (version v3.6-patch). *Notes Du Pole De Modelisation De Linstitut Pierre-simon Laplace (IPSL). Zenodo.*

Masina, S., Storto, A., Ferry, N., Valdivieso, M., Haines, K., Balmaseda, M., Zuo, H., Drevillon, M., and Parent, L. (2017). An ensemble of eddy-permitting global ocean reanalyses from the myocean project. *Climate Dynamics*, 49:813–841.

McPhee, M. (2008). *Air-Ice-Ocean Interaction: Turbulent Ocean Boundary Layer Exchange Processes*. Springer, Washington.

Mellor, G. and Ezer, T. (1995). Sea level variations induced by heating and cooling: An evaluation of the boussinesq approximation in ocean models. *Journal of Geophysical Research: Oceans*, 100(C10):20565–20577.

Merryfield, W., Holloway, G., and Gargett, A. (1999). A global ocean model with double-diffusive mixing. *Journal of Physical Oceanography*, 29(6):1124–1142.

Notz, D. and Worster, M. (2009). Desalination processes of sea ice revisited. *Journal of Geophysical Research: Oceans*, 114(C05006):1–10.

Nummelin, A., Ilicak, M., Li, C., and Smedsrud, L. (2015). Consequences of future increased arctic runoff on arctic ocean stratification, circulation, and sea ice cover. *Journal of Geophysical Research*, 121(1):617–637.

Nurser, A. and Bacon, S. (2014). The rossby radius in the arctic ocean. *Ocean Sci.*, 10:967–975.

Overland, J. E. and Wang, M. (2013). When will the summer arctic be nearly sea ice free? *Geophysical Research Letters*, 40(10):2097–2101.

Palmer, M., Roberts, C., Balmaseda, M., Chang, Y.-S., Chepurin, G., Ferry, N., Fujii, Y., Good, S., Guinehut, S., Haines, K., Hernandez, F., Köhl, A., Lee, T., Martin, M., Masina, S., Masuda, S., Peterson, K., Storto, A., Toyoda, T., Valdivieso, M., Vernieres, G., Wang, O., and Xue, Y. (2017). Ocean heat content variability and change in an ensemble of ocean reanalyses. *Climate Dynamics*, 49:909–930.

Pemberton, P., Nilsson, J., and Meier, M. (2016). Arctic ocean freshwater composition, pathways and transformations from a passive tracer simulation. *Tellus A: Dynamic Meteorology and Oceanography*, 68:1–21.

Persson, O. and Vihma, T. (2016). The atmosphere over sea ice. In Thomas, D., editor, *Sea ice*, pages 160–196. Wiley, Chichester.

Petrich, C. and Eicken, H. (2016). Overview of sea ice growth and properties. In Thomas, D., editor, *Sea ice*, pages 1–41. Wiley, Chichester.

Polyakov, I., Alekseev, G., Timokhov, L., Bhatt, U., Colony, R., Simmons, H., Walsh, D., and Zakharov, V. (2004). Variability of the intermediate atlantic water of the arctic ocean over the last 100 years. *J. Climate*, 17:4485–4497.

Polyakov, I., Pnyushkov, A., Alkire, M., Ashik, I., Baumann, T., Carmack, E., Goszczko, I., Guthrie, J., Ivanov, V., Kanzow, T., Krishfield, R., Kwok, R., Sundfjord, A., Morison, J., Rember, R., and Yulin, A. (2017). Greater role for atlantic inflows on sea-ice loss in the eurasian basin of the arctic ocean. *Science*, 356(6335):285–291.

Polyakov, I., Pnyushkov, A., and Carmack, E. (2018). Stability of the arctic halocline: a new indicator of arctic climate change. *Environmental Research Letters*, 13:1–8.

Proshutinsky, A., Aksenov, Y., Clement Kinney, J., Gerdes, R., Golubeva, E., Holland, D., Holloway, G., Jahn, A., Johnson, M., Popova, E., Steele, M., and Watanabe, E. (2011). Recent advances in arctic ocean studies employing models from the arctic ocean model intercomparison project. *Oceanography*, 24(3):102–113.

Proshutinsky, A., Krishfield, R., Timmermans, M.-L., Toole, J., Carmack, E., McLaughlin, F., Williams, W., Zimmermann, S., Itoh, M., and Shimada, K. (2009). Beaufort gyre freshwater reservoir: State and variability from observations. *Journal of Geophysical Research: Oceans*, 114(C1):1–25.

Proshutinsky, A., Steele, M., Zhang, J., Holloway, G., Steiner, N., Häkkinen, S., Holland, D., Gerdes, R., Koeberle, C., Karcher, M., Johnson, M., Maslowski, W., Zhang, Y., Hibler, W., and Wang, J. (2001). The arctic ocean model intercomparison project (aomip). *EOS*, 82(51):637–644.

Proshutinsky, A., Timmermans, M.-L., Ashik, I., B.-M. A., Carmack, E., Frolov, I., Krishfield, R., McLaughlin, F., Morison, I., Polyakov, I., Shimada, K., Sokolov, V., Steele, M., Toole, J., and Woodgate, R. (2012). The arctic (ocean) [in "state of the climate in 2011"]. *Bulletin of American Meteorological Society*, 93(7):S158–S163.

Proshutinsky, A., Yang, J., Krishfield, R., Gerdes, R., Karcher, M., Kauker, F., Koeberle, C., Hakkinen, S., Hibler, W., Holland, D., Maqueda, M., Holloway, G., Hunke, E., Maslowski, W., Steele, M., and Zhang, J. (2005). Arctic ocean study: Synthesis of model results and observations. *EOS*, 86:368–371.

Rainville, L., Lee, C., and R.A., W. (2011). Impact of wind-driven mixing in the arctic. *Oceanography*, 24(3):136–145.

Roy, I. (2018). Solar cyclic variability can modulate winter arctic climate. *Sci Rep*, 8(4864):1–15.

Rudels, B. (2009). Arctic ocean circulation. In Steele, J. H., editor, *Encyclopedia of Ocean Sciences (Second Edition)*, pages 211–225. Academic Press, Oxford, second edition edition.

Rudels, B. (2011). Arctic ocean circulation and variability - advection and external forcing encounter constraints and local processes. *Ocean Science Discussions*, 8:2313–2376.

Rudels, B. (2015). Arctic ocean circulation, processes and water masses: A description of observations and ideas with focus on the period prior to the international polar year 2007-2009. *Progress in Oceanography*, 132:22–67.

Rudels, B. (2016). Arctic ocean stability: The effects of local cooling, oceanic heat transport, freshwater input, and sea ice melt with special emphasis on the nansen basin. *Journal of Geophysical Research*, 121(7):4450–4473.

Rudels, B., Kuzmina, N., Schauer, U., Stipa, T., and Zhurbas, V. (2009). Double-diffusive convection and interleaving in the arctic ocean - distribution and importance. *Geophysica*, 45(1–2):199–213.

Sakov, P., Counillon, F., Bertino, L., Lisæter, K., Oke, P., and Korablev, A. (2012). Topaz4: an ocean-sea ice data assimilation system for the north atlantic and arctic. *Ocean Science*, 8:633–656.

Semtner, A. (1976). A model for the thermodynamic growth of sea ice in numerical investigations of climate. *Journal of Physical Oceanography*, 6:379–389.

Serreze, M. C. and Meier, W. N. (2018). The Arctic's sea ice cover: trends, variability, predictability, and comparisons to the Antarctic. *Annals of the New York Academy of Sciences*.

Shi, L., Alves, O., Wedd, R., Balmaseda, M., Chang, Y., Chepurin, G., Ferry, N., Fujii, Y., Gaillard, F., Good, S., Guinehut, S., Haines, K., Hernandez, F., Lee, T., Palmer, M., Peterson, K., Masuda, S., Storto, A., Toyoda, T., Valdivieso, M., Vernieres, G., Wang, X., and Yin, Y. (2017). An assessment of upper ocean salinity content from the ocean reanalyses inter-comparison project (ora-ip). *Climate Dynamics*, 49:1009–1029.

Shibley, N., Timmermans, M.-L., Carpenter, J., and Toole, J. (2017). Spatial variability of the arctic ocean's double diffusive staircase. *JGR Oceans*, 122(2):980–994.

Somavilla, R. (2019). Draining and upwelling of greenland sea deep waters. *JGR Oceans*, 124(4):2842–2860.

Steele, M., Zhang, J., and Ermold, S. (2010). Mechanisms of summertime upper arctic ocean warming and the effect on sea ice melt. *Journal of Geophysical Research*, 115(C11004):1–12.

Steiner, N., Holloway, G., Gerdes, R., Häkkinen, S., Holland, D., Karcher, M., Kauker, F., Maslowskie, W., Proshutinsky, A., Steele, M., and Zhang, J. (2004). Comparing modeled streamfunction, heat and freshwater content in the arctic ocean. *Ocean Modelling*, 6(3–4):265–284.

Steward, R. (2008). *Introduction to Physical Oceanography*. A & M University, Texas.

Storto, A., Masina, S., and Navarra, A. (2016). Evaluation of the cmcc eddy-permitting global ocean physical reanalysis system (c-glors, 19822012) and its assimilation components. *Q J R Meteorol Soc*, 142:738–758.

Stroeve, J., Serreze, M., Drobot, S., Gearheard, S., Holland, M., Maslanik, J., Meier, W., and Scambo, T. (2008). Arctic sea ice extent plummets in 2007. *EOS*, 89(2):13–14.

Talley, L., Pickard, G., Emery, W., and Swift, J. (2011). *Descriptive Physical Oceanography: An Introduction*. Academic Press, London, UK.

Tietsche, S., Balmaseda, M., Zuo, H., and Mogensen, K. (2015). Arctic sea ice in the global eddy-permitting ocean reanalysis orap5. *Climate Dynamics*.

Timmermans, M.-L. and Jayne, S. (2016). The arctic ocean spices up. *Journal of Physical Oceanography*, 46:1277–1284.

Toyoda, T., Fujii, Y., Yasuda, T., Usui, N., Ogawa, K., Kuragano, T., Tsujino, H., and Kamachi, M. (2016). Data assimilation of sea ice concentration into a global ocean-sea ice model with corrections for atmospheric forcing and ocean temperature fields. *J Oceanogr*, 72(2):235–262.

Uotila, P., Goosse, H., Haines, K., Chevallier, M., Barthélemy, A., Bricaud, C., Carton, J., Fučkar, N., Carric, G., Iovino, D., Kauker, F., Korhonen, M., Lien, V., Marnela, M., Massonnet, D., Mignac, D., Peterson, K., Sadikni, R., Shi, L., Tietsche, S., Toyoda, T., Xie, J., and Zhang, Z. (2018). An assessment of ten ocean reanalyses in the polar regions. *Climate Dynamics*, pages 1–38.

Uotila, P., Holland, D., Maqueda, M., Häkkinen, S., Holloway, G., Karcher, M., Steele, M., Yakovlev, N., Zhang, J., and Proshutinsky, A. (2005). An energy-diagnostics intercomparison of coupled ice-ocean arctic models. *Ocean Modelling*, 11(1-2):1–27.

Valdivieso, M., Haines, K., Zuo, H., and Lea, D. (2014). Freshwater and heat transports from global ocean synthesis. *J Geophys Res Oceans*, 119:394–409.

Warner, T. (2011). *Numerical Climate and Weather Prediction*. Cambridge University Press, Cambridge, UK.

Woodgate, R. (2013). Arctic ocean circulation: Going around at the top of the world. *Nature Education Knowledge*, 4(8):8.

Woodgate, R. A., Aagaard, K., Muench, R., Gunn, J., Bjork, G., Rudels, B., Roach, A., and Schauer, U. (2001). The arctic ocean boundary current along the eurasian slope and the adjacent lomonosov ridge: Water mass properties, transports and transformations from moored instruments. *Deep Sea Research Part I: Oceanographic Research Papers*, 48(8):1757–1792.

Xie, J., Bertino, L., Counillon, F., Lisæter, K. A., and Sakov, P. (2017). Quality assessment of the topaz4 reanalysis in the arctic over the period 1991-2013. *Ocean Sci*, 13(1):123–144.

Yang, J. (2006). The seasonal variability of the arctic ocean ekman transport and its role in the mixed layer heat and salt fluxes. *Journal of Climate*, 19:5366–5387.

Zhang, J. and Rothrock, D. (2000). Modeling arctic sea ice with an efficient plastic solution. *J. Geophys. Res*, 105:3325–3338.

Zhang, J. and Steele, M. (2007). Effect of vertical mixing on the atlantic water layer circulation in the arctic ocean. *Journal of geophysical research: Oceans*, 112:1–9.

Zuo, H., Balmaseda, M., and Mogensen, K. (2015). The new eddy-permitting orap5 ocean reanalysis: description, evaluation and uncertainties in climate signals. *Climate Dynamics*.

Zuo, H., Balmaseda, M. A., Tietsche, S., M.-K., and Mayer, M. (2019). The ecmwf operational ensemble reanalysis-analysis system for ocean and sea-ice: a description of the system and assessment. *Ocean Sci*, 15:779–808.

Appendix A. Per grid trends in T and S for the layer 0–100 m

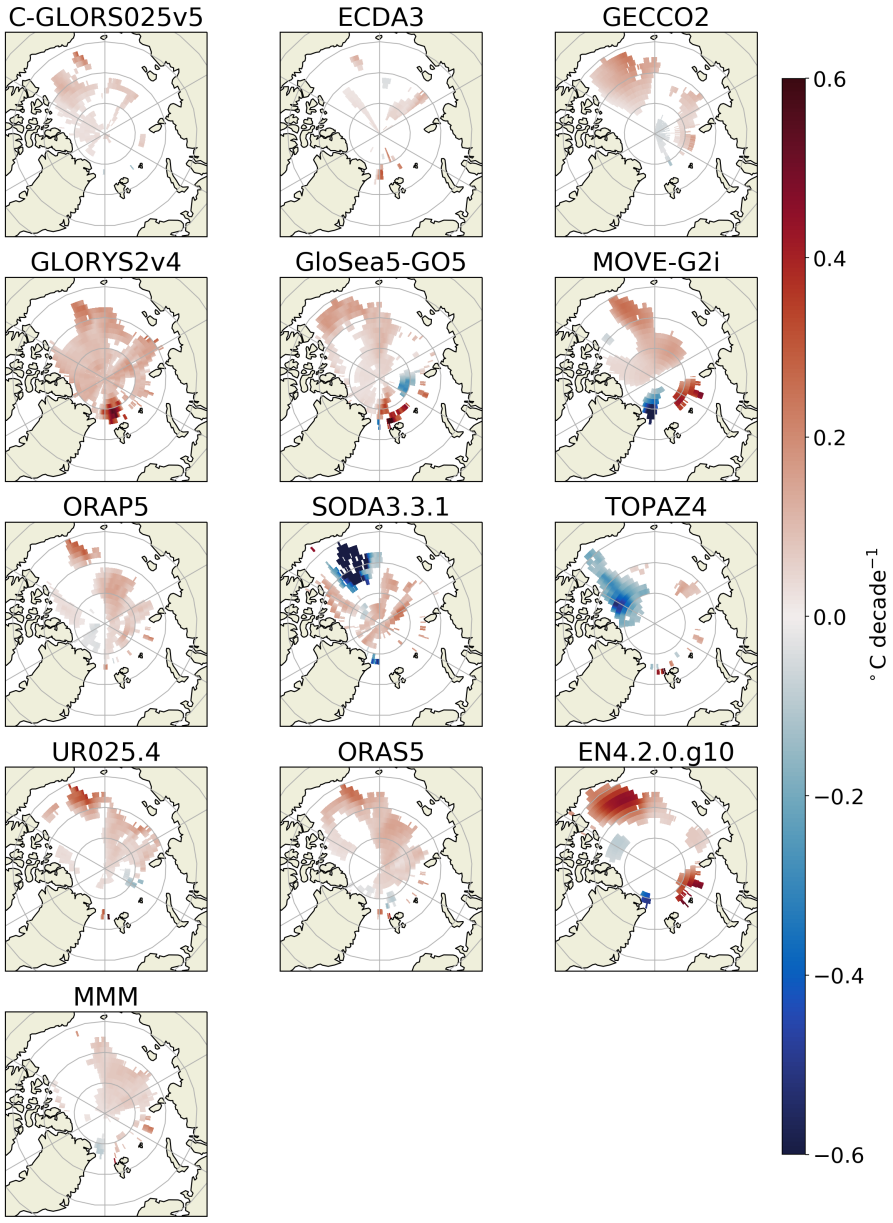

Figure A.1: Significant changes in temperature for the layer 0–100 m.

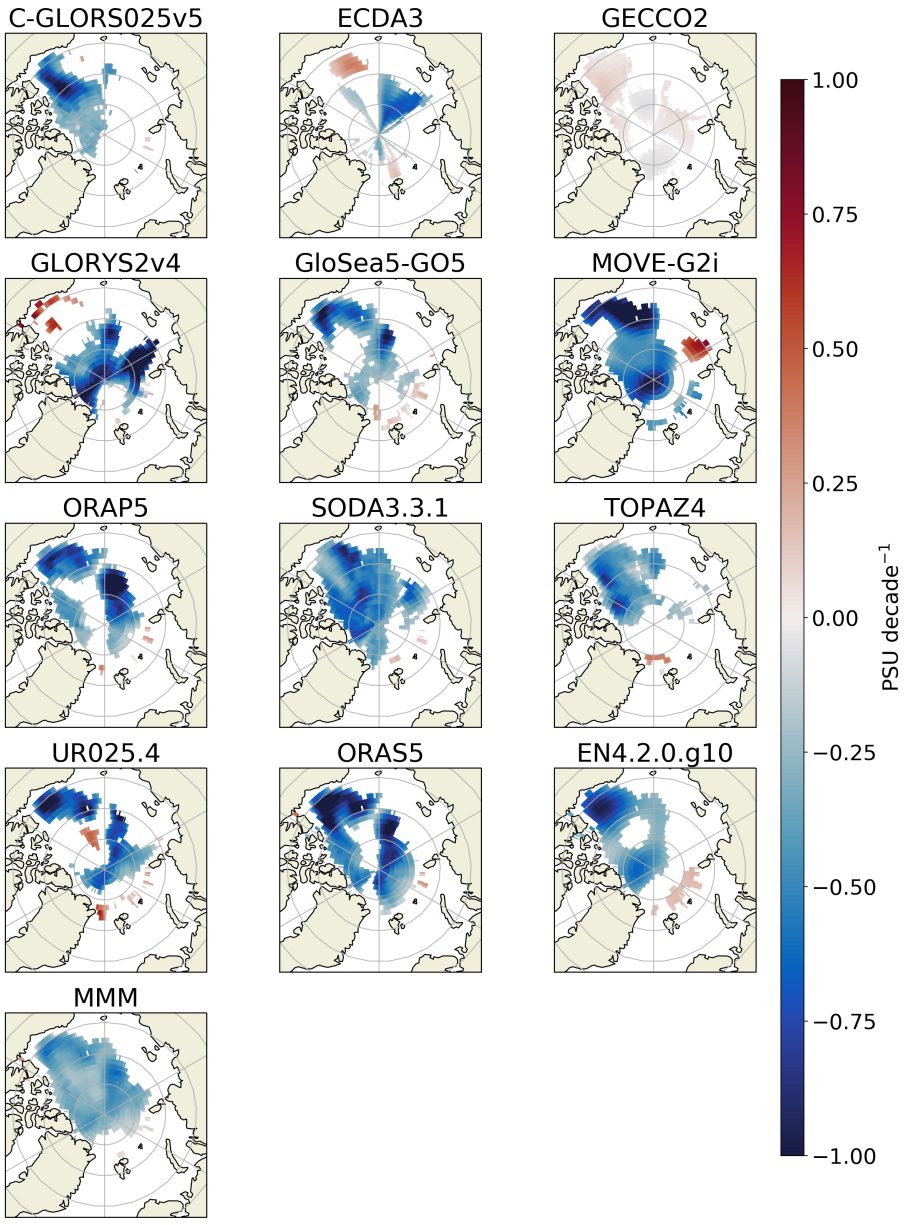

Figure A.2: Significant changes in salinity for the layer 0–100 m.